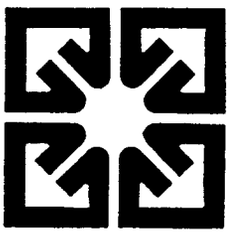

SUPERCOMPUTER COMPUTATIONS RESEARCH INSTITUTE

SIMULATION STUDIES OF TRACKING SYSTEMS AT VERY HIGH LUMINOSITY

by

D. Adams, F. Bird, D. Coupal,
M.J. Corden, D. Xiao, P. Estabrooks,
W.T. Ford, R. Hamatsu, K. Kondoh,
G. Hanson, F. Luehring,
B. Hubbard, W.S. Lockman,
K. O'Shaughnessy, A.M. Lee, B. Zou,
A. Palounek, H. Ziock, G. Trilling

FSU-SCRI-95-112

November 1995

THE FLORIDA STATE UNIVERSITY
TALLAHASSEE, FLORIDA

Simulation Studies of Tracking Systems at Very High Luminosity[†]

D.Adams
Bonner Nuclear Laboratory, Rice University

F.Bird, D.Coupal
Superconducting Super Collider Laboratory

M.J.Corden, D.Xiao
Supercomputer Computations Research Institute, Florida State University

P.Estabrooks
Dept of Physics, Carleton University

W.T.Ford
Dept of Physics, University of Colorado

R.Hamatsu, K.Kondoh
Dept of Physics, Tokyo Metropolitan University

G.Hanson, F.Luehring
Dept of Physics, Indiana University

B.Hubbard, W.S.Lockman, K.O'Shaughnessy
Institute for Particle Physics, University of California, Santa Cruz

A.M.Lee, B.Zou
Dept of Physics, Duke University

A.Palounek, H.Ziock
Los Alamos National Laboratory

G.Trilling
Lawrence Berkeley Laboratory

Abstract

Detailed computer simulation studies of a tracking detector originally designed for high luminosity operation at the Superconducting Super Collider have been carried out. Detector simulation and track reconstruction techniques appropriate to the extremely high charged particle rates corresponding to luminosities of up to 10^{34} $cm^{-2}s^{-1}$ are described. The detector performance is evaluated and compared to design requirements stemming from the physics goals of the SDC experiment. The results have implications for the design of tracking detectors at future high luminosity hadron colliders such as the Large Hadron Collider (LHC).

[†]Submitted to *Nucl. Inst. & Meth.*

1 Introduction

Charged particle tracking and momentum measurement were fundamental components of the Solenoidal Detector Collaboration (SDC) experiment, which was planned for the Superconducting Super Collider (SSC).

The extremes of energy and luminosity needed to accomplish the physics goals of the SSC made unprecedented demands on tracking systems, which needed to cope with charged particle rates over the whole detector of 10 GHz and above. Extensive direct testing of all the detector components was necessary; however, the only practical way to carry out design studies of the collective performance of the whole system under SSC conditions was by computer simulation, using the measured or anticipated properties of individual components as input. This paper describes detailed simulation studies of the SDC baseline tracking system, including comparison of alternative design options. The studies were carried out at the SSC center of mass energy of 40 TeV, for luminosities up to ten times the nominal design luminosity of 10^{33} $cm^{-2}s^{-1}$.

Charged particle tracking is also an integral part of both the major experiments planned for the Large Hadron Collider (LHC) at CERN. The LHC will try to address the physics questions left unanswered by the cancellation of the SSC project. The lower centre of mass energy of 14 TeV will be compensated by placing even more emphasis on achieving the highest possible luminosity, with a design target of 10^{34} $cm^{-2}s^{-1}$, the same as the maximum luminosity considered in the present study. The tracking technologies which were part of the SDC baseline design and which form the subject of this paper, are all under consideration for incorporation into the two major high p_t experiments at the LHC [2, 3]. The studies of the high luminosity performance of the tracking technologies described in the following sections are of direct and immediate relevance to LHC experiments. Indeed, much of the simulation software developed within the SDC collaboration and described below is already being applied to the simulation of tracking detectors which have been proposed for the LHC[4].

1.1 SDC detector overview

The SDC detector was designed around a large, superconducting solenoidal coil of effective radius 1.84 m, length 8.3 m and central field 2 Tesla. The tracking system occupies the region inside the coil, up to a maximum radius of 1.65 m. Outside the coil is a scintillating tile calorimeter, followed by a muon detector incorporating magnetized iron toroids.

The SDC baseline charged particle tracking system is illustrated in fig. 1a. It consists of inner barrel and forward disk systems of silicon microstrip detectors covering the pseudorapidity interval $|\eta| < 2.5$, surrounded by a cylindrical system of straw drift tubes covering $|\eta| < 1.8$, and an intermediate-angle tracking detector (ITD) consisting of gas microstrip detectors covering $1.8 < |\eta| < 2.5$.

An alternative design was also studied, in which the silicon microstrip system remained as described above, but the outer straw tube and gas microstrip systems were replaced by a cylindrical system of scintillating fibers covering the pseudorapidity interval $|\eta| < 2.25$. The corresponding layout is shown in fig. 1b. Some basic parameters of the subdetector systems of both designs are listed in table 1. In the table, the term "superlayer" represents two or more closely-spaced sensing layers within a single structural element. These superlayers are described in detail in section 3.

Small angle stereo is used to measure z, the axial coordinate, for all of the central subdetectors, and r, the radial coordinate, for the forward ones. The individual detectors are discussed in more detail in section 3 in the context of detector simulation. Further technical information about the proposed SDC tracking system may be found in the SDC Technical Design Report [1] and references

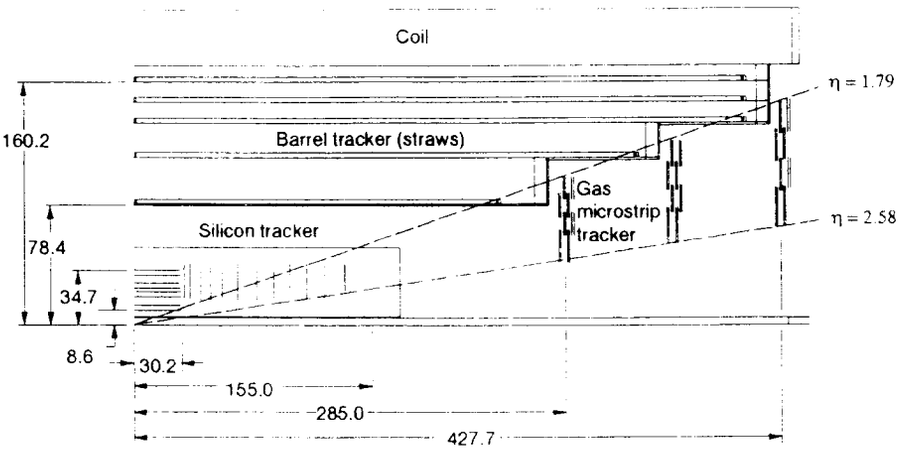

(a)

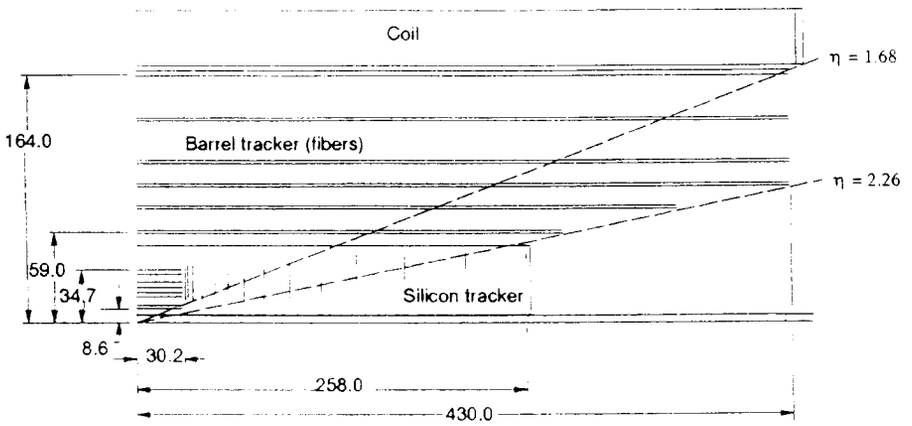

(b)

Figure 1: a) SDC baseline charged particle tracking system; b) Tracking system with scintillating fiber outer tracker.

Table 1: Summary of detector parameters

Subdetector	straw tubes	scint. fibers	silicon barrel	forward silicon	gas microstrips
no. of superlayers	5	6	8	2 × 13	2 × 6
no. axial measurements on track	24	24	8	7	6
no. stereo measurements on track	12	8	8	7	6
stereo angle	±3°	±6°	10 mrad	≤10 mrad	±100 mrad
minimum radius (cm)	82	60	9	15-40	35-51
maximum radius (cm)	163	165	35	39-46	79-116
minimum $\|z\|$ (cm)	0	0	0	33	285
maximum $\|z\|$ (cm)	241-403	300-430	30	258	427
number of channels	137K	475K	2.3M	4.2M	1.4M

therein.

1.2 SDC tracking detector design requirements

A set of design requirements was established for the SDC tracking system, based on the physics aims of the experiment [1]. The performance goals relevant to this study that can be tested by simulation are listed below:

1) Full acceptance over the pseudorapidity interval $|\eta| \leq 2.5$. This is particularly motivated by the need to achieve good geometrical acceptance for the Higgs boson decay $H \rightarrow Z^0 Z^0 \rightarrow l^+l^- l^+l^-$. The acceptance for all four leptons to have $|\eta| \leq 2.5$ is approximately 55% for a Higgs mass $M_H = 300$ GeV/c^2, and increases with increasing M_H.

2) Resolution in p_t, the transverse momentum perpendicular to the beam direction, of $\sigma(p_t)/p_t^2 < 0.2$ (TeV/c)$^{-1}$ for energetic, isolated charged tracks with $|\eta| \leq 1.8$, which may rise to 1.0 (TeV/c)$^{-1}$ at $|\eta| = 2.5$. This is important for many purposes. It should permit the reconstruction of the Z^0 mass with a resolution comparable to the natural width, and the charge determination for leptons from massive W pairs or from a Z' of mass up to 4 TeV/c^2.

3) Reconstruction efficiency for isolated, $p_t \geq 10$ GeV/c tracks of $\geq 97\%$ at design luminosity, with ≤ 0.1 fake tracks of $p_t \geq 10$ GeV/c per trigger. This is fundamental for the detection of many rare processes and heavy particles that can give rise to isolated, energetic tracks, such as Higgs boson or top quark production.

4) Reconstruction efficiency $\geq 90\%$ for isolated tracks at 10 × design luminosity. This would permit searches for new, heavy particles with particularly low production cross sections, such as a Z' or some forms of Higgs, up to the highest possible luminosities.

5) Reconstruction efficiency $\geq 80\%$, with $< 10\%$ fakes, for tracks of $p_t \geq 5$ GeV/c within jets of p_t up to 100 GeV/c. This would allow the tagging of b and c quarks by the reconstruction of

muons in jets.

6) Position resolution extrapolated to the calorimeter shower maximum detector of $\leq$ 5 mm in $r\phi$ (where bremsstrahlung smearing occurs) and $\leq$ 2.5 mm in z, to achieve good background rejection for electron identification.

7) Resolution $\leq$ 2 mm for the track z coordinate at the primary vertex, in order to separate the triggering event from background interactions.

1.3 Simulation objectives

The primary goal of the simulation was to measure the performance of the complete tracking system, in terms of momentum and position resolution and reconstruction efficiency. This was used to optimize the cost/performance ratio of the tracker, consistent with meeting the design requirements. However, there were also more specific goals, for example:

1) calculation of particle fluxes in various parts of the detector;

2) determination of sensitivity to high backgrounds, such as unexpectedly large neutron fluxes;

3) sensitivity to damage, hardware inefficiencies and dead channels;

4) comparison of alternative detector technologies, for example, straw tube and scintillating fiber trackers.

The study of these and related questions is described in the following sections.

1.4 Outline of the paper

The simulation studies may be broken down naturally into stages corresponding to the principal sections below. The computational work for all of these was incorporated within a modular framework called SDCSIM, developed within the Solenoidal Detector Collaboration.

Section 2 describes the general simulation parameters and tools used, including event generators. The detailed simulation of the various SDC tracking subdetectors is described in section 3. The track reconstruction algorithms are explained in section 4. Some rate calculations and performance characteristics not depending on the complete track reconstruction are given in section 5, and section 6 presents the main results on tracking system performance for physics processes. The conclusions of the study are summarized in section 7.

2 Detector simulation overview

The simulation is built around the ubiquitous GEANT Monte Carlo program [5]. It is divided into three parts: event generation; a particle transport phase, where particles are tracked through the detector, taking account of decays and interactions with matter, including energy loss by ionization, multiple Coulomb scattering, nuclear interactions and explicit delta ray production; and a "digitization" phase, in which the signals observed in the active elements of the detector itself are simulated and recorded. Both primary and secondary particles are tracked until either they leave the detector, their energy falls below a threshold of 1 MeV for electrons and gammas or 10 MeV for hadrons or muons, or the elapsed time is too great for any further contribution to the recorded digitizations for the triggering event. The digitizations correspond as closely as possible to the data that would be read out from the actual detector. They are written to a file for eventual input to the event reconstruction program.

The SDCSIM framework provides an interface that allows particles from a variety of event generators to be used as input to GEANT, as described below. The geometrical model of the

SDC detector and the detailed simulation of the detector response were developed within the collaboration, and are described separately in section 3.

2.1 Event generators

At high luminosities, it is not sufficient to generate just the physics event of interest; the additional "minimum bias" background events that occur during the detector sensitive time, also known as pileup, must also be generated. At the SSC design luminosity of 10^{33} cm^{-2}s^{-1}, there would be an average of 1.6 proton-proton interactions per bunch crossing, at a bunch crossing rate of 60 MHz. These additional interactions are superimposed on the interaction of interest (the "trigger" interaction) and complicate the task of track reconstruction in several ways: the 1.6 interactions in the same crossing produce additional "in-time" tracks; the sensitive time of some detector elements is greater than the 16 ns between crossings, and so interactions from neighboring bunch crossings also contribute to the recorded data; and low p_t tracks trapped by the solenoidal magnetic field ("looping" tracks) from previous bunch crossings survive long enough to overlap with the crossing of interest. All these effects are included in the simulation.

The physics processes studied in this report were simulated with the ISAJET event generator [6]. For the particular case of Higgs boson production, events were generated with a Higgs boson of nominal mass 300 GeV/c^2 decaying into a pair of Z bosons, one of which decays into e^+e^- and the other into $\mu^+\mu^-$. In the following text, these are referred to simply as "Higgs events."

For operational reasons, a separate generator was used to produce the low Q^2 "minimum bias" background events, which were superimposed on the physics processes of interest. We used PYTHIA [7], tuned to produce 7.2 charged particles per unit rapidity per non-diffractive event [8].

In order to limit the computational requirements, only those generated tracks with $|\eta| \leq 3.5$ were tracked through the detector, and only interactions occurring between 6 crossings before and 2 crossings after the triggering beam crossing were simulated. This is sufficient to cover the sensitive times of all the SDC detector elements, and gives most of the hits produced by the looping tracks from previous crossings. These limitations were lifted for the determination of rates and occupancies at design luminosity described in section 5.1.

The number of interactions generated at design luminosity is determined for each beam crossing by drawing a random number from a Poisson distribution with a mean of 1.6. Higher luminosities are simulated by scaling the mean of the Poisson distribution accordingly, for example, 5 $\times$ design luminosity requires an average of 5 $\times$ 1.6 = 8 minimum bias events per bunch crossing. A Gaussian shape was assumed for both transverse and longitudinal dimensions of the interaction region, with standard deviations of 10 μm and 5 cm respectively.

3 Detector representation and response

3.1 Simulation of silicon microstrip detectors

The barrel module of the silicon microstrip detector is composed of 8 layers of 6 cm long double-sided wafers, which are bonded together in pairs to form 12 cm long readout units. The strip pitch is 50 μm on both sides of the wafer. The strips on one side of the wafers are axial, whereas those on the reverse side have a 10 mrad stereo angle. There is an inactive border region of 600 μm at the edges and the ends of each wafer. The wafers are 300 μm thick, and are tilted at an angle of 7.5° to the radial direction, to partly compensate for the Lorentz angle.

In the forward region, the 6 cm long wafers are wedge shaped and also bonded into 12 cm readout units, as shown in fig. 2. The radial strips are numbered sequentially in ϕ, with a pitch ranging

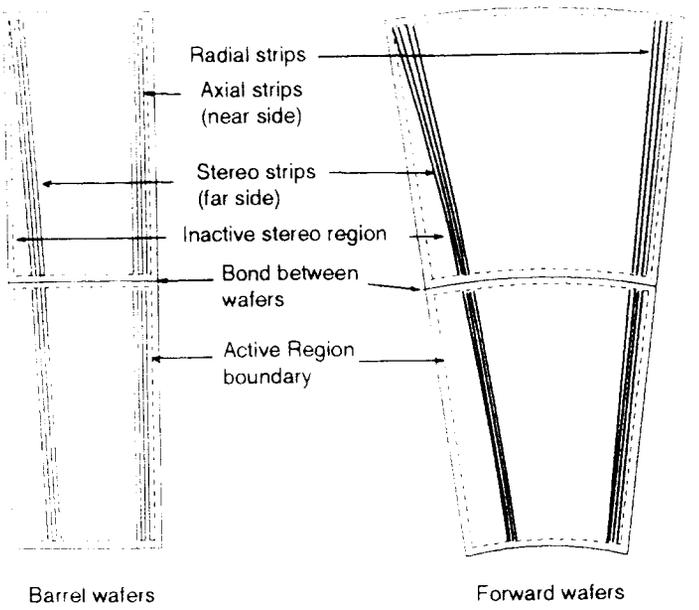

Figure 2: Barrel and forward wafers of silicon microstrip system.

from 28 to 58 μm over the radial extent of the unit, to give a ϕ uncertainty that is independent of r. On the reverse side, the stereo strips are also tapered and have an effective stereo angle of 10 mrad at the outer edge. In order to achieve uniform resolution over the surface of a wafer for the r coordinate measurement, these strips are not straight but logarithmic spirals, where the radial coordinate is given by

$$r = r_{edge} + p(N_r - N_{st})/\tan\mu$$

where N_r and N_{st} are the radial and stereo strip numbers, μ is the stereo angle and p is the pitch, all at the outer edge of radius r_{edge}. Adjacent units are staggered in z to reduce dead space and to leave space for cables.

The support and cooling systems are not simulated in full detail; instead, they are represented by additional inert material at each layer. The whole silicon detector is contained within a beryllium gas enclosure vessel. The mean fraction of a radiation length for the barrel at normal incidence is 0.06 (see also fig. 7 of section 3.5). Each silicon wafer is represented by a separate GEANT "sensitive" volume, a box for the barrel or a trapezoid for the forward regions, with its own individual rotation matrix. For each wafer, a list of four near neighbors is kept. This substantially reduces the search time for tracking a particle through the entire silicon system.

During the tracking phase, each time a charged particle traverses a silicon wafer, the entry point, exit point, time and deposited energy are recorded in a temporary store. In the digitization phase, for each particle passing through a wafer, the deposited energy is shared between strips according to the path length beneath each strip, assuming uniform deposition along the path length. The energy deposits beneath each strip are summed within a sensitive time interval of 20 ns, centered on the nominal time of arrival of a relativistic particle from the triggering beam crossing. If the sum exceeds a discriminator threshold of 30 KeV, approximately one third of the energy deposited by a minimum ionizing particle, a recorded hit or "digitization" is stored for that strip. A strip has a deadtime of 64 ns following a hit, during which time no further digitizations can be recorded. Contiguous hit strips are then grouped into clusters, (in the actual experiment, this would happen on-line); only the cluster position and width are read out. No pulse height information is recorded,

either in the digitization or the final readout.

The distribution of cluster widths is shown in fig. 3a for events containing jets. There are more one-strip than two-strip clusters, and there is a tail extending to large numbers of strips due to particles travelling in the plane of a detector wafer. The effects on the charge flow of diffusion and of the magnetic field, the latter effect significant in the barrel region only, are not included. These effects would be expected to increase the number of two-hit clusters, without significant impact on the position resolution. Noise hits and electronic inefficiencies are not simulated for the silicon system.

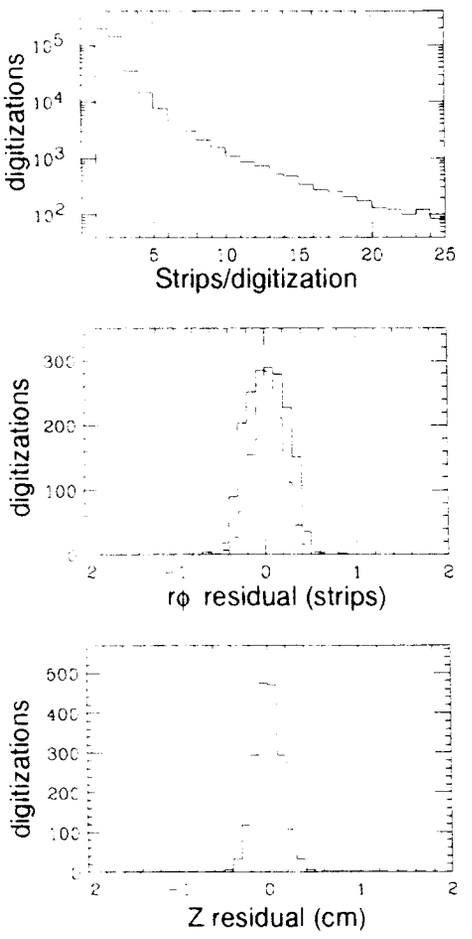

Figure 3: top: Number of silicon strips in cluster; middle: Fitted track residuals in $r\phi$ for clusters in the barrel silicon detector. The solid (dashed) histogram is for single (double) strip clusters; bottom: z residuals in the barrel silicon detector.

The position resolution as determined from track fit residuals is shown in figs. 3b and 3c. For single hit clusters, the azimuthal resolution in $r\phi$ is 10 μm in the barrel detectors. This is 30% better than $p/\sqrt{12}$ (the naive estimate from the strip pitch p, assuming only single hit clusters), since particles near the boundary cause hits in two strips. In the forward detectors, the resolution is slightly worse, since usually only one strip is hit. Similarly, the resolution in the longitudinal coordinate (z for barrel, r for forward) is 1.5 mm, compared with the naive estimate of $(p/\tan\mu)/\sqrt{6} = 2$ mm.

3.2 Simulation of straw tubes

The straw drift tube system consists of five concentric "superlayers," each supported by a carbon fiber epoxy and foam laminate cylinder, and divided into separate halves at the $z = 0$ median plane. The odd-numbered superlayers consist of 8 layers of close-packed straw tubes, of maximum length 4 meters, parallel to the beam axis. Superlayers 2 and 4 contain 6 layers of straw tubes at stereo angles of $+3°$ and $-3°$, respectively. The geometrical properties of the system are summarized in fig. 1a and table 1.

In the baseline tracking system design, the straw tubes are enclosed in trapezoidal carbon fiber epoxy and foam laminate shells to form modules [9]. In the simulation, to limit the computation time, the axial straws are positioned directly on the surface of the support cylinders, and the stereo straws at their midpoint are tangential to the cylinders. The material of the carbon fiber modules and the straw tube walls is represented by a layer of inert material adjacent to each straw tube layer. The total number of radiation lengths for the 5 superlayers of straw tube modules and their supporting cylinders is 0.044 at normal incidence. The material in the region between the straw and gas microstrip detectors associated with straw module endplates, cables, support frame, *etc.*, is included explicitly in the simulation. It can be seen as a peak in the plot of number of radiation lengths against rapidity in fig. 7 of section 3.5. Its effect on electron identification is discussed in section 6.5.

The two detector halves, the superlayers and the straw layers are all represented by individual volumes in GEANT. Each axial layer is represented by a cylindrical shell, and a new type of GEANT volume, a hyperboloid, was created to represent the envelope of a stereo layer. The outer radius of the volume representing each layer is reduced slightly to avoid overlapping the start of the next layer, because of the packing of the straws.

When a charged track crosses a layer, the GEANT program determines the entry and exit points. From these, the list of straw tubes traversed is obtained, and the distance of closest approach of the particle to each wire is calculated. This is stored separately for each tube, along with timing, position along the wire and other data, and is known as a "hit." Hits are accumulated for all tracks from all interactions in all beam crossings simulated in conjunction with a single trigger event.

The signals recorded by the detector for each wire, or "digitizations," are then computed. Each hit is checked to see whether the track passes through the sensitive region of the straw. The exact wire positions, straw tube sizes, wall thicknesses and inter-straw gaps are used. Plastic wire supports give rise to dead regions of length 0.6 cm at 80 cm intervals along the wire. For structural reasons, the supports are at the same z in all layers of a superlayer, which can lead to a correlated loss of hits within the superlayer. In addition, 2% of hits are discarded randomly to simulate straw tube and electronic inefficiencies from various sources excluding geometric acceptance and deadtime. The recorded time is computed from the distance of closest approach to the wire, using a linear time-distance relationship and an effective drift velocity of 70 μm/ns in the 2 Tesla magnetic field. (This corresponds to a drift velocity of roughly 100 μm/ns with no field for the projected CF_4 - isobutane gas mixture. It is assumed that small non-linearities can be calibrated out in the final system.) The recorded time is corrected for the particle time of flight, the beam crossing time relative to the triggering beam crossing and the signal propagation time along the wire, and is smeared by the expected resolution of 150 μm. The latter is increased beyond the expected intrinsic straw resolution of 100-120 μm resulting from fluctuations in ionization cluster formation, electron diffusion, *etc.*, to allow for a contribution from alignment uncertainties and possible electronic noise effects. The resulting time spectrum of hits for the inner superlayer for minimum bias events, prior to any shadowing effects, is shown in fig. 4a, and discussed further in section 5.1.

All the hits on a single wire are time-ordered to facilitate calculation of deadtime losses. A

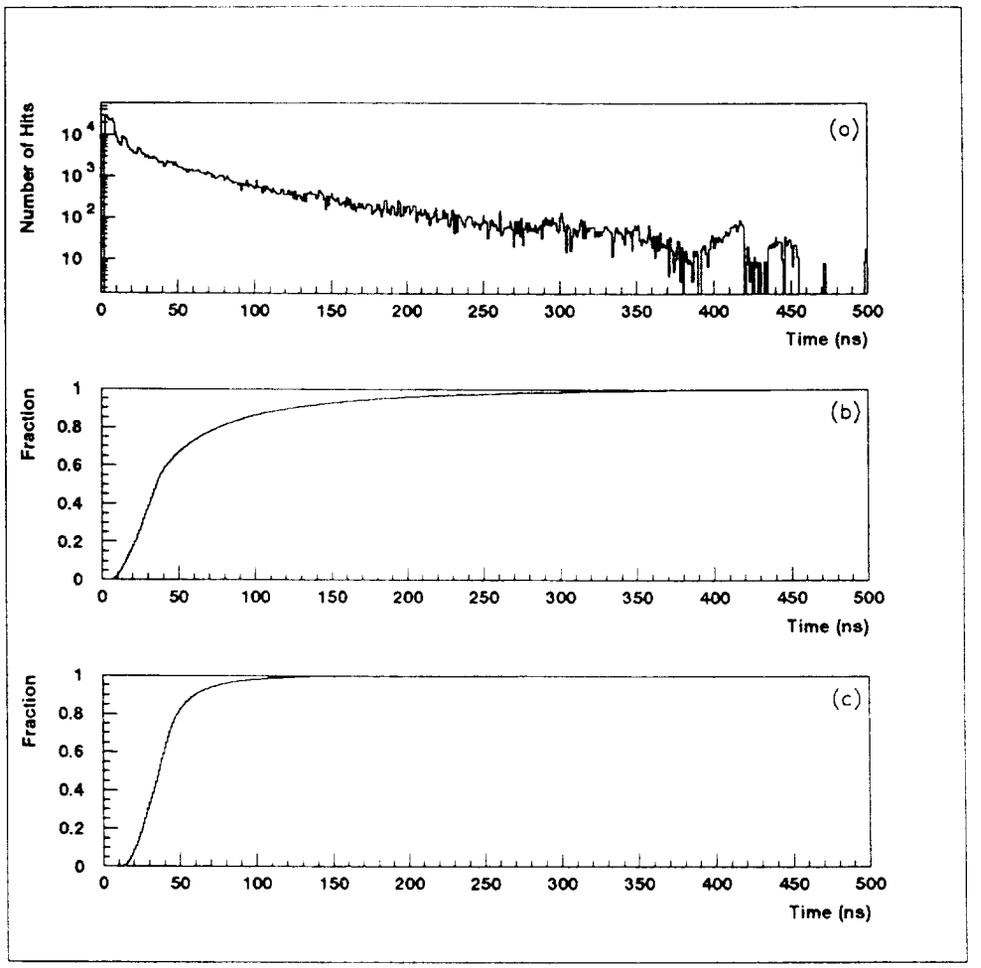

Figure 4: a) Time spectrum for hits in the innermost straw superlayer, from minimum bias events without shadowing. b) fraction of hits occurring before a given time, *i.e.*, integral of a); c) fraction of hits for outer superlayer.

conservative double-pulse resolution of 40 ns is estimated from convoluting the electronics shaping time with the maximum drift time of just under 30 ns. Any hit occurring less than 40 ns after an earlier hit is "shadowed" and is not recorded, even if the earlier hit was itself shadowed. All unshadowed hits falling within a time gate of width 50 ns after the triggering beam crossing are recorded by the simulation, although a slightly narrower, superlayer-dependent time window is imposed for event reconstruction. A hit falling within the time gate may be shadowed by a hit that precedes the gate. In the limit of infinite luminosity, no digitizations would be recorded, because all hits would be shadowed by another hit in the preceding 40 ns. An example of shadowing is illustrated in fig. 5, where an early, looping track ("looper") crosses a high-momentum muon. For the looper, the small circles represent the actual distance of closest approach of the track to each wire. The large circles represent the recorded (digitized) time. Where the outer loop crosses the muon track, the recorded time for the looper is smaller than the time that would be recorded for the muon, which is near the outside of the straw. The muon hit is therefore shadowed by the looper and is not recorded. A looper hit from this layer has been incorporated in the reconstructed track segment (solid line), distorting it slightly. However, the effect on the fully reconstructed track (dashed line) is negligible.

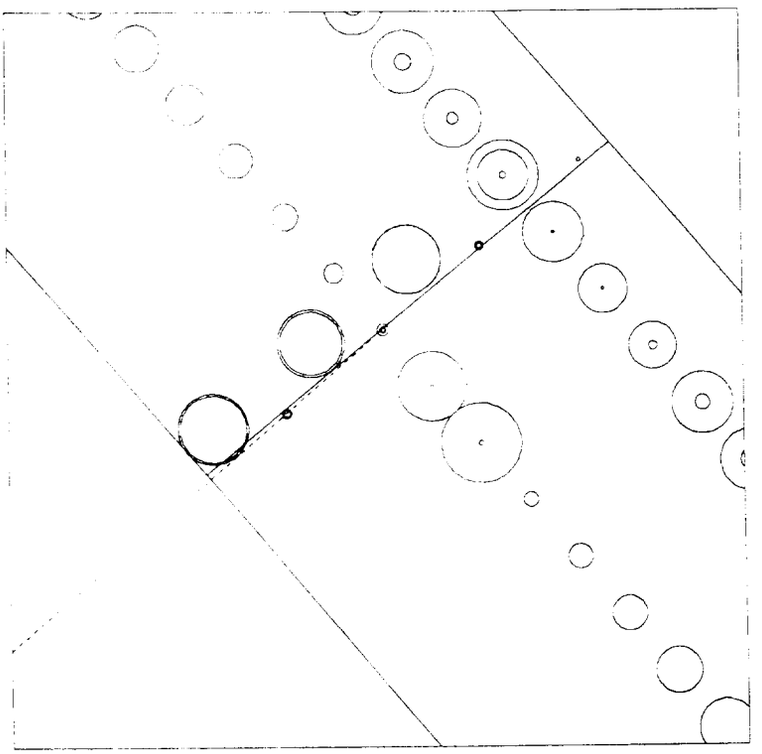

Figure 5: Example of an in-time hit shadowed by a looping track. The inner circles represent the pure drift time alone, hence the spatial position of the track. The outer circles represent the measured time including the time offset of the primary interaction and the particle time of flight. The dashed and solid lines represent the reconstructed track and track segment respectively.

Effects due to the ambient neutron and photon background are also included at the digitization stage. The background straw tube rates have been calculated to be 40 Hz/cm for neutrons and 160 Hz/cm for photons at the design luminosity of 10^{33} $cm^{-2}s^{-1}$ [10], assuming an average of 1.3 straw hits per interacting neutron and 2 per photon. Random noise hits at this rate are generated

uniformly over the detector. The additional deadtime losses due to the longer pulse widths from photons and especially neutrons (about 100 ns) have been simulated by increasing the random straw inefficiency. Both extra hit rates and inefficiencies are proportional to the luminosity.

3.3 Simulation of gas microstrips

Each half of the gas microstrip intermediate-angle tracker consists of 6 superlayers, grouped into 3 pairs, as may be seen in an $r - z$ view in fig. 1a. Each superlayer consists of a carbon fiber-foam disk supporting radial/stereo pairs of wedge shaped detector tiles arranged in 4 annuli, with alternating annuli on opposite sides of the support disks, as illustrated in fig. 6. Each member of a pair of superlayers has the same tile structure (number of annuli, number of tiles per annulus, tile size, *etc.*), but each annulus of the second superlayer is rotated azimuthally by half a tile to avoid overlaps of the dead areas at the sides of the tiles. The strip pitch varies from 200 to 500 μm, and the stereo angle is 100 mrad. The dead areas at the edges of the tiles (approximately 6 mm at inner and outer edges and about 3 mm on each side) are included in the simulation. Stereo tiles are described in the same way as the radial ones, a simplification that slightly overestimates the dead area at the corner of each stereo tile.

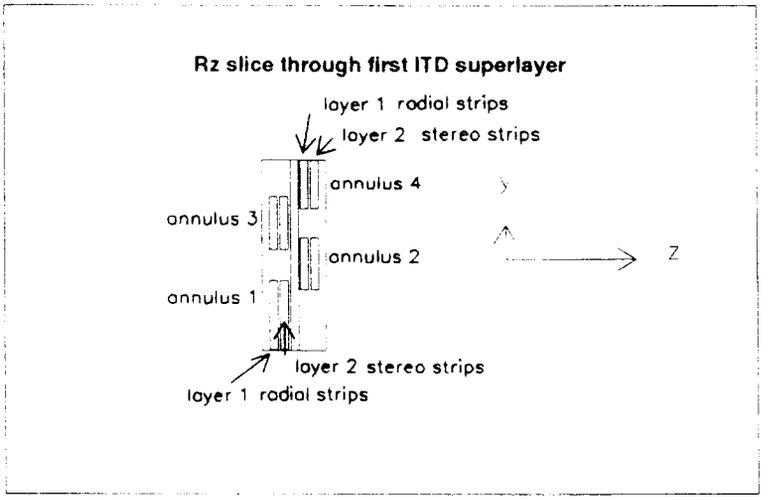

Figure 6: Side view of annuli within a gas microstrip superlayer.

Each tile is simulated as a uniform chunk of material, *i.e.*, the detailed mechanical structure is not simulated, but the total amount of material in the tile is correct. The readout electronics, cables, *etc.*, are assumed to be located at the inside of each annulus, and the corresponding material is included in the simulation. Gas ionization, drift properties, *etc.*, are not simulated in detail. The mean fraction of a radiation length for the simulated gas microstrip system alone is about 10% (15% for regions of overlapping tiles) for each end. Each individual gas microstrip tile is represented by a separate GEANT "sensitive" volume, a trapezoid, with its own individual rotation matrix.

During the tracking phase, each time a charged particle traverses a gas microstrip tile, the entry point, exit point, deposited energy, time with respect to the beam crossing, tile number and Monte Carlo track and vertex numbers are recorded as a "hit." In the digitization phase, for each such hit, the deposited energy is shared between anodes according to the path length through the tile, assuming uniform deposition along the path length. The energy deposits on each anode are

summed within a sensitive time interval of 20 ns, centered on the nominal time of arrival of a relativistic particle from the triggering beam crossing. However, if there has been a "hit" on the same anode within a time interval of 65 ns before the start of the sensitive time, the current hit is not recorded. If the energy sum exceeds an (adjustable) discriminator threshold of approximately one tenth of that of a minimum ionizing particle, a recorded hit or "digitization" is stored for that strip. The simulated readout is purely digital, with no pulse height information recorded. Effects of the gas ionization and drift have been neglected. With the expected drift velocity of approximately 100 μm/ns and a gap of 3 mm between the drift plane and anode-cathode plane, the maximum drift time is 30 ns. However, for reasonably high-p_t tracks the first electrons will arrive at the anode at times ranging from zero to a few ns after the passage of the particle and about one third of the electrons will arrive within the first 10 ns, so the main effect of neglecting the drift time will be that the occupancy is somewhat overestimated.

A 4% random inefficiency is included to simulate dead channels and other non-geometric effects. The expected rate of random noise hits, from sources such as the ambient neutron background, is very small. The position resolution resulting from the strip pitch and cluster size is in the range 50-100 μm in $r\phi$ and 0.5-1.0 mm in r, depending on the position along the strip.

3.4 Simulation of scintillating fibers

The alternative SDC outer tracker design, shown in fig. 1b, has scintillating fibers arranged in six cylindrical superlayers at radii of 60, 76, 92, 108, 136 and 165 cm, supported by carbon fiber epoxy and foam laminate cylinders. The outer four superlayers have a half-length of 430 cm and the inner two are shorter; the inner three all cover the range $|\eta| < 2.25$. The fibers are circular with an active diameter of 0.870 mm, and are laid out on ribbons with a center-to-center spacing of 1.0 mm. They are broken at the middle and are read out on both ends of the detector (*i.e.*, not at $\eta = 0$).

Two radially adjacent layers of scintillating fibers are offset by a half-fiber spacing in $r\phi$, so that the gaps in one layer lie next to the fiber centers in the next, and constitute a "doublet." The spatial resolution of a doublet for an isolated radial track, obtained from the simulation, is 110 microns, which is consistent with simple geometrical estimates. All superlayers include two doublets of fibers parallel to the beam axis, with a radial separation of 1.8 cm. In addition, the third and the sixth superlayers each have two opposite-sign stereo doublets in which the fibers trace a helix with a pitch of 6°. The stereo doublets are positioned immediately outside the outer axial doublet.

The individual fibers are not defined as GEANT volumes. Instead, each of the axial doublets is described by a cylindrical shell with a thickness of 3.0 mm, except for the outer doublets of the two stereo superlayers, for which a thickness of 7.0 mm is used to include the one axial and two stereo doublets. The material is plastic (CH) with a radiation length of approximately 40 cm. At normal incidence, the total material in the scintillating fiber system alone is 0.10 radiation lengths (see fig. 7 of section 3.5).

As GEANT tracks particles through the detector, each intersection with the cylinders of scintillating fibers is recorded as a hit, and the position and energy loss are stored. In the subsequent digitization phase, a fraction of the energy deposited in each step is assigned to a fiber according to the fraction of the step path length that intercepts that fiber. The expected number of detected photons for the fiber is proportional to this energy and is exponentially attenuated by the distance to the readout end of the fiber. Parameters were chosen such that a minimum ionizing particle passing at normal incidence through the fiber center at the readout end would produce 8.4 photons at the photodetector, whereas if the same traversal occurred at the end opposite to the readout ($\eta = 0$), 5.4 photons would reach the photodetector. Energetic particles from the interaction point

strike the readout end of the fiber ($|\eta| = 2.25$) at a steep angle, which increases the path length in the fiber, and increases the number of photons at the photodetector from 8.4 to approximately 40.

The actual number of detected photons is selected from a Poisson distribution, and the time of detection is the sum of the beam crossing time, the particle time of flight from the primary interaction to the fiber, the time to propagate down the fiber at 20 cm/ns and the scintillator response time. For each photon, the response time is chosen randomly from an exponential distribution with a characteristic time of 7.8 ns. The discriminator output for each fiber is turned on for 16 ns starting at the time each photon is received. Thus, the system is continuously updated and has no deadtime. Each fiber is sampled once per bunch crossing, at a slightly different time for each superlayer, and if a signal is present, the fiber is recorded as ON. With these parameters, a track typically contributes to two bunch crossings, since the time between crossings is only 16 ns.

Dead channels were simulated by turning off 1% of the fibers at random. Neutron background is expected to be the primary source of noise hits, and these were simulated for each event by randomly turning on 0.5% of the channels at design luminosity (10^{33} cm^{-2}s^{-1}), and scaling linearly for other luminosities (*e.g.*, 5% at 10^{34} cm^{-2}s^{-1}).

3.5 Material representation

The SDC tracking system, though well matched to SSC physics, has intrinsically more material than previous collider tracking systems. This is a consequence of the small cell size needed to cope with high luminosities and of the large acceptance required for SSC physics.

The material in the tracking system results in some degradation of trigger performance and of off-line reconstruction and identification of electrons and photons. Electron bremsstrahlung in the tracking material will degrade the electron momentum resolution both off-line and in the level-one tracking trigger. This in turn smears the trigger p_t threshold, and reduces the efficiency of off-line electron identification when the reconstructed momentum is required to match the visible energy in the calorimeter. Bremsstrahlung may also distort the position measurement and lateral shower profile in the electromagnetic calorimeter, impeding electron identification. Photon conversion results in background to the electron trigger, and some inefficiency in the high-p_t photon trigger. It is important to simulate the material in the tracking system accurately in order to quantify the above effects, and to minimize them by distributing the material in the system in an optimal way.

To verify the representation of material in the simulation, we used the program RTRACE, developed within the collaboration. RTRACE is a ray tracing package based on GEANT geometries, which operates within the SDCSIM framework. It is useful for direct studies of the distribution of material, and quick, parametric studies of detector performance based on geometry and material content alone. RTRACE will calculate thicknesses in terms of radiation lengths or nuclear absorption lengths, as well as purely geometric quantities. These may be summed over any chosen parts, subsets or groups of detectors, and plotted as a function of azimuthal angle ϕ and pseudorapidity η or polar angle θ. The calculations are performed by tracking non-interacting, massless neutral particles through the detector, starting from a chosen vertex and using a grid of values of η and ϕ, and updating the sums at each boundary.

Figs 7a and 7b show the total numbers of radiation lengths of material in the models of the tracking system used for the simulation of the two major design options, as a function of pseudorapidity. The figures agree with calculations made directly from engineering drawings of the detector. In fig. 7a, the thickness of material for the whole tracking system varies between about 11% and 25% of a radiation length, except for a spike in the region $1.6 < |\eta| < 1.9$ corresponding to the straw superlayer endplates and associated electronics. Fig. 7b shows that the scintillating fiber design has more material in the barrel region, but it does not have the spike around $|\eta| = 1.8$.

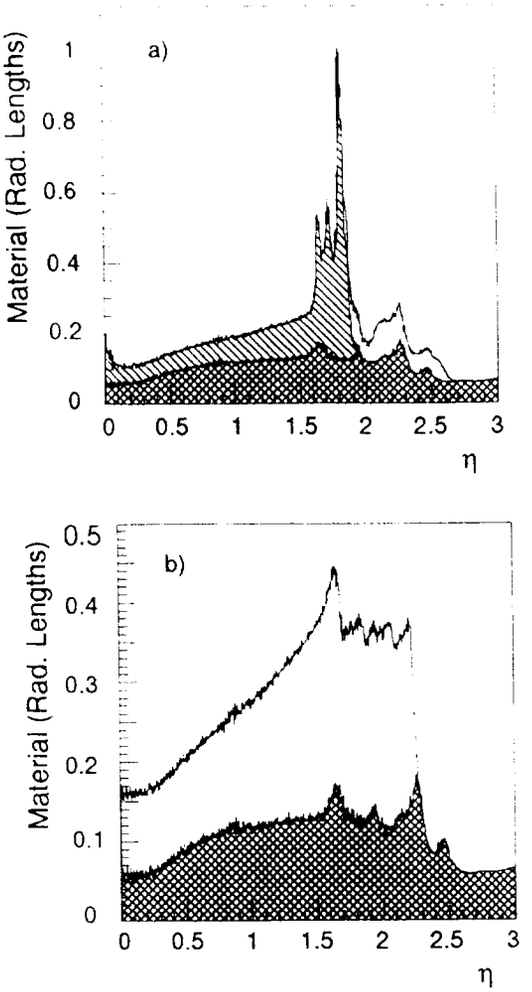

Figure 7: Thickness of material in the tracking system as a function of pseudorapidity for a) the straw/ITD version, and b) the scintillating fiber version. The double hatching corresponds to the silicon tracker, the unhatched region represents the gas microstrips in a) and the scintillating fibers in b), and the single hatching in a) represents the straw tubes.

(Fig. 7b does not include certain supports that are beyond the $|\eta| < 2.25$ limit of the scintillating fiber acceptance.) The effects of the material on electron reconstruction are discussed in sections 6.5 and 6.6.

4 Reconstruction algorithms

The reconstruction phase of the simulation can be logically divided into two stages: one that produces detector subsystem-specific quantities, such as space points or track segments; and one that links the information from all tracking subdetectors to find complete tracks. To some degree, the choice of output for the first stage is determined by the particular algorithm used for overall track finding in the second stage. For historical reasons related to the various subsystems, several different algorithms were developed. Although time-consuming, this redundancy was useful, since comparisons of the results of different algorithms helped to differentiate between performance limitations due to the design of the tracking system and ones due to the choice of pattern recognition algorithm.

4.1 Definitions and overview

In order to combine the information from the various tracking systems, it is necessary to define common track parameters. We adopt the standard SDC coordinate system, in which the x axis points towards the center of the SSC ring, y points upwards, and z points in one beam direction such that the system is right-handed. Because of the cylindrical symmetry of the detector, the corresponding cylindrical coordinate system is commonly used: r is the radius relative to the beam direction (z axis), and ϕ is the azimuthal position in the $x-y$ plane.

All algorithms discussed here assume a uniform magnetic field, so that a track trajectory may be described by a simple helix. We choose to specify the parameters of the helix at the point of closest approach of the track to the origin in the $x-y$ plane, as illustrated in fig. 8 and defined below: ϕ_0 is the azimuthal direction of the track in the $x-y$ plane when extrapolated back to the point of closest approach to the origin; λ is the angle between the track direction and the $x-y$ plane; b_0 is the distance to the origin in the $x-y$ plane at the point of closest approach, with the convention that b_0 is positive if the coordinate origin lies inside the helix, and negative otherwise; z_0 is the distance to the origin in z at the point of closest approach in the xy plane; ρ is the track curvature (inverse radius of curvature); and p_t is the transverse momentum with respect to the beam direction.

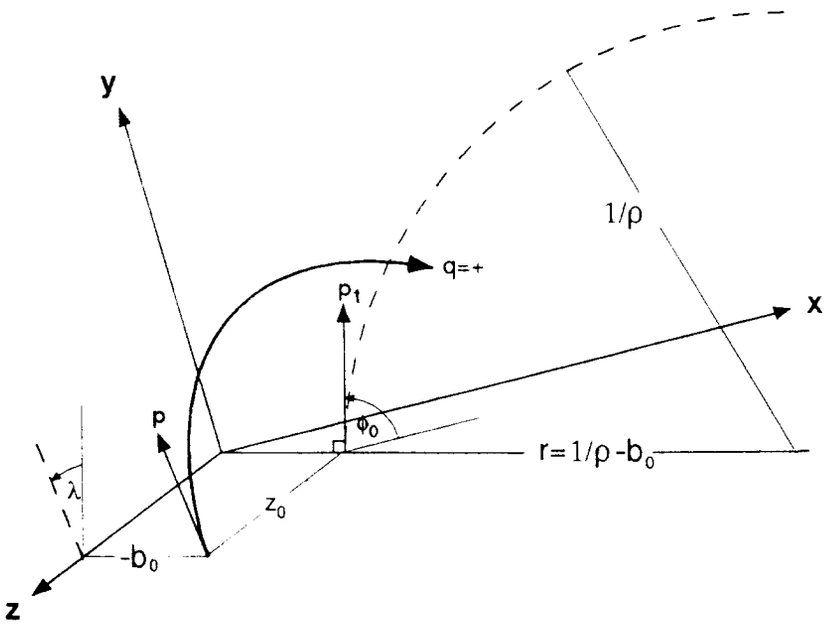

Figure 8: Parameters used to describe tracks and track segments.

4.2 Space point and segment reconstruction in silicon strips

4.2.1 Space points

Since clustering of contiguous hit strips is carried out on-line, cluster parameters are read out and are directly available for reconstruction. Clusters on the axial side of a wafer are matched with clusters on the stereo side to obtain three-dimensional space points. Due to the small stereo angle of 10 mrad, a stereo strip typically crosses only 24 axial strips along the length of a readout unit.

Because of the small strip area, the occupancy is low, (see section 5.2 and table 2), and consequently there is little ambiguity in the matching of stereo and axial clusters, about 10% at a luminosity of 3×10^{33} cm^{-2}s^{-1}. All possible matching combinations are kept; unmatched axial clusters are also retained. The space points and errors are stored in the global cylindrical coordinate system described in section 4.1. The position errors are taken to be

$$d\phi = \frac{p}{\sqrt{12}\, r}$$

$$d(long) = \frac{p}{\sqrt{6}\, \tan\mu} ,$$

where r is the radius at which the pitch p is defined and *long* is the longitudinal coordinate: z for the barrel and r for the forward modules. The stereo angle is μ. The covariance term is set to:

$$covar(long\ \phi) = \frac{p^2}{12\ r\ \tan^2\mu} .$$

4.2.2 Segments

Local track vectors, also known as track segments, are constructed from space points in two adjacent silicon layers. Each adjacent layer pair is treated as a superlayer and searched for segments. A simple algorithm matches a coordinate in an inner layer with the coordinate nearest in ϕ in the next layer. If there is more than one possible match within a road in ϕ corresponding to $p_t > 0.8$ GeV/c for tracks originating from the beam axis, then up to 3 combinations are kept, with preference given to the segments with highest p_t. The segments are characterized by the track parameters at the origin of the transverse plane, ϕ_0, z_0, ρ and λ, to facilitate subsequent track finding. A search for segments is made in all superlayers. A single space point may thus contribute to segments in two different layer pairs. Any duplicate space points are eliminated after segment linking during the track fit.

4.3 Segment reconstruction in straw tube superlayers

The precision of a single measurement in the straw layers is about an order of magnitude poorer than that of a silicon layer. A straw measurement also has a twofold (right-left) ambiguity, and lower efficiency because of deadtime losses in the larger detector unit. These limitations are compensated by the superlayer organization of the straw detector. Each superlayer provides enough closely-spaced measurements to permit reliable and unambiguous local reconstruction of track segments. This leads also to a substantial reduction in the data passed to the global track finding program.

The time measurement in the straw tubes can be converted into a simple circular contour of distance from the wire, to which the trajectory is tangent. This fact is not altered by the magnetic bending of the drift electron trajectory, but it is assumed that the arrival time of the signal at the readout electronics is given solely by the drift time. In fact, variations in arrival time due to particles striking different parts of the wire are not entirely negligible. They result from differences in the particle time of flight and in the propagation time for the signal pulse to reach the readout end of the wire, and are typically the time equivalent of about 100μm of track displacement, comparable to the intrinsic resolution. In the segment finder we treat the track crossing time as a parameter to be inferred from the segment fit, along with the azimuth and direction of the track. A Gaussian constraint with uncertainty corresponding to the range of track arrival delays is included in the fit.

The segment finder considers one superlayer at a time. For example, an axial superlayer has layers numbered 1 to 8 from the interaction point outward. The outermost program loop searches

layers 8, 7, 6 and inwards for a first hit, the starting point for a candidate segment. The next loop, nested within the first, searches layers 1, 2, 3 and outwards for a hit with azimuthal angle ϕ not too different from that of the first hit. For this pair of hits we have four choices of right/left ambiguity, and each is taken as a seed for the segment. This search order maximizes the hit separation so that each seed segment has a well determined direction.

The segment is interpolated in turn to each of the layers falling between those of the seed hits. Each new layer is searched for a hit within a window of the interpolated segment, taking account of the left-right ambiguity for any new hit. When one is found, a least-squares fit to the augmented list of hits is performed. If the fit passes a χ^2 test, it provides an updated set of the segment parameters incorporating the new hit, which defines the road for continuation to the next layer.

The search continues through all of the internal layers, with a χ^2 test and parameter update at each stage. When the layers and hits are exhausted, enough having been successfully linked, we review the ambiguity assignments of all internal hits, refitting and selecting the best choice according to the χ^2. The candidate is then saved temporarily until all four right/left choices for the seed have been considered. Finally the (up to four) candidates are compared. The test variable is: $(N_{layers} - N_{hits})^2 + \chi^2/dof$, where dof is the number of degrees of freedom. The candidate with the smallest value of this test variable is accepted as a segment.

Hits on the segment are excluded from further consideration as the search for more segments proceeds. This means that not all possible combinations get considered, and errors can occur because of an unlucky choice of the search order. We compensate for this in a simple manner: the program is organized so that it can be called repeatedly with the minimum number of hits as an input argument. A loop executes searches with minimum hit levels of 8, 7, ..., forcing the program to favor segments with high numbers of hits, at some cost in computer time. The results in section 5.3 and elsewhere were obtained with an absolute minimum of four hits per segment.

4.4 Space point and segment reconstruction in the gas microstrip ITD

The recorded ("digitized") data for the gas microstrips, like the silicon strip data, consists of cluster centers and widths, not individual microstrips. Pattern recognition proceeds in the same way as for the silicon microstrips. Clusters in adjacent (radial and stereo) layers are associated to form space points ("coordinates"). Pairs of nearby coordinates in adjacent superlayers that point back to the interaction point in both the $r - \phi$ and $r - z$ planes, within tolerances, are then combined to make track segments. These segments can be used subsequently by either the the zonal track finding or the segment clustering algorithm discussed below.

4.5 Segment clustering track finding

This method finds tracks by searching for clusters of silicon or gas microstrip track segments with similar track parameters. Fig. 9a shows a region of (ϕ_0, ρ) space containing track segments and their errors. Segments from the same track overlap each other, as illustrated in a highly magnified region of the space in Fig. 9b, and a χ^2 association can be used to make clusters from the segments. A similar scheme is used in the $(\tan\lambda, z_0)$ plane. The χ^2 contributions from (ϕ_0, ρ) and $(\tan\lambda, z_0,)$ clustering are combined before testing for the compatibility of a segment with a given cluster. The track candidate then consists of the space points contributing to the track segments in the cluster, after removal of duplicates. The weighted means of the segment parameters provide starting values for the track fit.

The clustering is performed independently for the barrel and forward segments, as they are described by different parameters. If a track goes through both the barrel and the forward geometry,

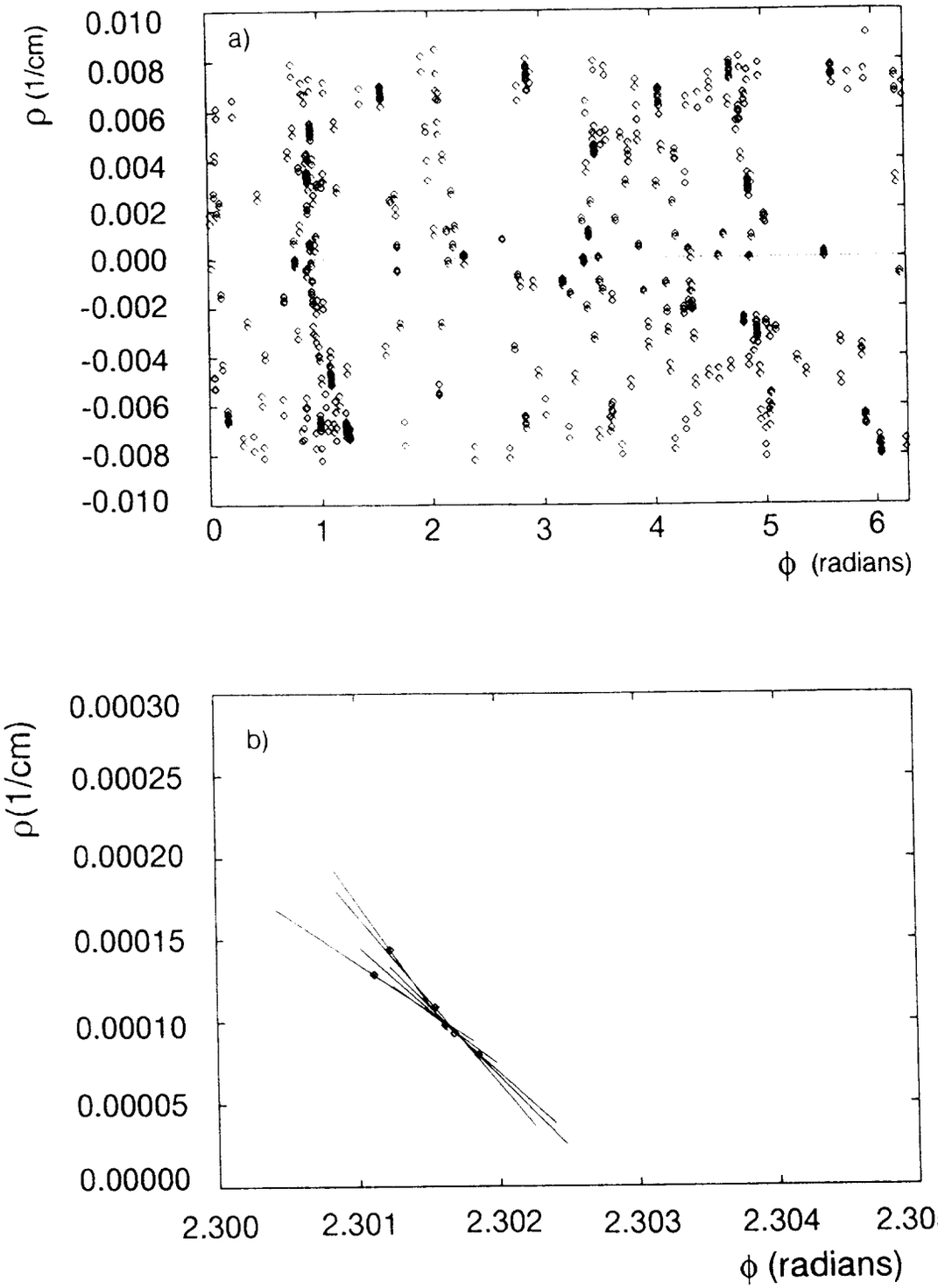

Figure 9: Distribution of barrel silicon segments in the (ϕ_0, ρ) plane from a single Higgs event: a) whole event; b) single track.

both candidate track stubs are passed on to the track fitting stage. Each is extrapolated into the other region using a road technique (see section 4.8).

The algorithm could in principle include straw segments also. However, the uncertainties on the segment parameters extrapolated back to the origin are much larger for the straw segments, due to both the lower intrinsic resolution of the straw system and the longer extrapolation distance. This results in the silicon segments from more than one track being associated with the same straw segment, and spoils the effective two-track resolution. Therefore, in the region $|\eta| < 1.8$, track segment clustering is carried out in the silicon detector only. At a later stage, track candidates are extrapolated out into the straw tube tracker, where straw segments are matched locally.

Finally, there is an attempt to resolve clusters containing many segments, where tracks are very close together, such as in jets. These large clusters are subdivided into smaller ones with a maximum of one segment per layer pair. Resulting track candidates with a minimum number of segments, usually three, are passed on to the fitting stage.

4.6 Zonal track finding

This track finding algorithm uses as input the reconstructed track segments described in the preceding sections. The segments from each subdetector enter on an equal footing, weighted by the appropriate errors. Each track segment may be characterized locally by three measured parameters: ϕ, the azimuthal position of the center of the segment; α, the angle between the track segment and the radial direction; and z, the longitudinal position of the segment. Under the assumption that the segment forms part of a track that passes through the coordinate origin in the transverse plane, α can be replaced by the signed inverse radius of curvature, $\rho = 2\ (\sin\alpha)/r$, where r is the radius of the segment measurement. Similarly, z may be replaced by

$$\lambda = \tan^{-1}(0.5\rho z/\alpha) \quad \approx \tan^{-1}(z/r) \quad ,$$

the dip angle between the segment and the transverse plane.

Track finding zones are defined using curvature ρ, dip angle λ, and azimuthal direction at the origin ϕ_0. They cover the entire angular acceptance of the SDC tracker, and curvatures in the range $|\rho| < 0.75m^{-1}$. These track zones are curved in space: the zone limits in ϕ are calculated separately for each superlayer from the superlayer radius, zone curvature and ϕ_0 limits. The zones overlap sufficiently that at least one zone will contain all the segments belonging to any detectable track with $p_t > 1.0$ GeV/c. An example of overlapping zones is shown in fig. 10, (not to scale). When testing whether a segment curvature falls within a zone, the zone width is extended by 3 times the uncertainty in the segment curvature. The axial straw superlayers do not measure z, and so zones cannot be defined in λ for the corresponding segments. For stereo superlayers, the width of the zone in ϕ is extended to allow for the dependence on the (unknown) z of the segment. After a segment is assigned to a zone, a rough estimate of z and hence λ is made from the difference between the ϕ of the stereo segment and the ϕ of the center of the zone.

The algorithm decides if a zone contains a track by counting the number of superlayers in the entire tracking system that contain a segment within the zone. Typically, a zone with 5 or more occupied superlayers is considered a track candidate.

The algorithm considers only track zones starting at the transverse coordinate origin. This works for primary tracks, since a coordinate system can be chosen centered on the small transverse beam spot, but it limits the ability of the algorithm to find secondary tracks from long lived decays or photon conversions. An extension of the algorithm to find such tracks is possible. In the longitudinal direction, it has not been found necessary to subdivide zones according to the z

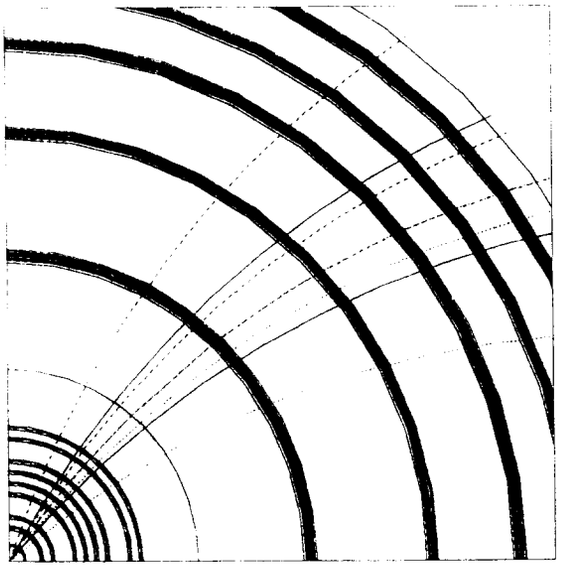

Figure 10: End view of a low-p_t track passing through the overlapping zones used in the zonal track finding method. Solid, dashed, and dotted zone outlines are used to help distinguish between overlapping zones.

position of the interaction point to allow for the ± 5 cm variation expected at the SSC, although such an extension of the algorithm would be straightforward.

For reasons of computational efficiency, zones are not made as small as the detector resolution. Also, the special problems of matching straw tube stereo segments require the zone limits to be widened in straw stereo superlayers. Therefore, a candidate zone may contain more than one potential track. If more than a minimum number of superlayers, usually four, have two or more segments within the zone, the zone is subdivided until the subzones contain at most one track each.

Because the zones are deliberately overlapped for maximum efficiency, the same track may be found in more than one zone. At the end of the track finding, track candidates are compared and duplicates eliminated. Two tracks are considered duplicates if they have at least 50% of their segments in common. Only the track with segments in the largest number of superlayers is retained. Finally, if a track candidate has more than one possible segment in a single superlayer, a simple helix fit is used to pick the best one.

4.7 Reconstruction in the scintillating fiber tracker

The reconstruction method for the fiber tracker described here does not make use of space points or segments, but it uses clusters from each fiber doublet directly in a three-dimensional road-following track-finding algorithm. The superlayers of the scintillating fiber tracker are laid out in such a way that a segment based algorithm would also be possible.

4.7.1 Clustering

In each layer of a fiber doublet, adjacent hit fibers are merged to form clusters. Overlapping clusters in the two layers are then combined to form superclusters. The position of a supercluster is taken to be midway between the outermost contributing fibers. If the supercluster contains not more than one fiber in either layer, it is assumed to result from a single track, and assigned an error

of $0.5 \times s/\sqrt{12}$, where s is the center-to-center fiber spacing within each layer. Otherwise, it is assumed to result from multiple tracks and is assigned an error of $w/\sqrt{12}$, where the supercluster width w is the distance between the outer edges of its outermost fibers.

4.7.2 Track finding by road following

The road following method searches for tracks along predefined paths through the entire tracking system starting from the vertex and working outwards through the silicon microstrips and scintillating fibers. The search is begun with a seed track with very large errors. Every time a cluster or supercluster is added to the track, the track parameters and errors are updated using a Kalman filter algorithm [11]. An attempt is made to extend the track to each of the nearby clusters in each layer, and if this attempt is successful (*i.e.*, the χ^2 is sufficiently small), then a new track is created with the updated parameters. Thus one track may branch into many when a layer is added. Tracks are eliminated when they fail to pick up clusters in two adjacent or any three layers. At the end, tracks that share a large number of clusters are merged.

This method works well for a system where there are a relatively small number of measurements (here 20-30), each with high efficiency. In this case, a high reconstruction efficiency can be maintained while rapidly eliminating tracks that fail to pick up clusters in a small number of silicon layers or fiber doublets. This is important to minimize the number of track candidates and thus maintain acceptable computing performance. The method automatically provides a fit of the tracks at each position in the detector and takes into account the effects of multiple scattering.

4.8 Track fit

An iterative least squares fit is used to determine the five track parameters ϕ_0, λ, b_0, z_0 and ρ, defined in section 4.1. The input to the fit consists of starting estimates for the track parameters and a list of measurements that belong to the track. Optionally, this may include the transverse beam position as an extra constraint. For the segment clustering method of track finding, the initial estimate for b_0 is zero, and the remaining parameter starting values are taken from the center of the cluster. For the zonal track finding, starting parameter values are obtained from a simple fit to the segments of the track candidate. The measurements to be fitted differ according to the subsystem, but, in each case, axial and stereo measurements are kept separate. For the silicon strips or gas microstrips, the fitted measurement is the center of a cluster of hit strips. For the straw system, the measurement is the segment position at the radial midpoint of a superlayer. The error matrix includes contributions from multiple scattering in the material between each pair of measurements, as well as the measurement errors themselves.

An initial fit is made and a χ^2/dof is calculated. If this is greater than a cutoff value, the measurements that contribute most to the χ^2 are deleted one at a time until the cut is satisfied or the minimum number of measurements is reached.

A road algorithm then searches for additional measurements not initially associated with the track. Easier regions of the detector are searched before difficult ones; for example, interpolation is preferred to extrapolation. Measurement layers crossed by but not contributing to the track are searched one at a time, and a road is calculated using the current fitted parameters and their errors at the closest track point. Any measurement within the road, (or the nearest to the road center if there is more than one), is added to the track. The track is refit each time a new measurement is added, and the measurement is retained provided the track still satisfies the χ^2 cut. The procedure is repeated until all possible measurement layers that do not already contribute to the track have been searched. It is possible for two separate track stubs to be independently extended to give two

Table 2: Occupancies and charged particle rates per channel at design luminosity

Subdetector	Charged particle rate/channel	Occupancy
silicon tracker		
(inner barrel superlayer)		0.3%
(forward superlayers)		0.05%
gas microstrips	300 kHz	0.3%
scintillating fibers		
(inner superlayer)		2.8%
(outer superlayer)		0.8%
straw tubes		
(inner superlayer)	4.3 MHz	11.6%
(outer superlayer)	0.9 MHz	2.8%

longer tracks containing almost the same hits. When all tracks have been fitted, a search is made for such duplicate tracks, and the one with fewer hits is deleted.

5 Intermediate results

5.1 Charged particle rates

The charged particle rates in the various parts of the detector have been calculated from the simulation of minimum bias events, as described in section 2.1. They depend on the detector cell size and location, and take account of secondary interactions, particles trapped by the magnetic field, and decays.

Looping tracks can cause hits in the detector for up to 0.5 μs after they are generated. This is illustrated for the case of the straw tracker in fig. 4a, which shows the time spectrum for hits from in-time minimum bias events. Tracks are followed for a full 500 ns for the rate calculations described in this section. Comparison of figs. 4b and 4c shows that late hits occur preferentially in the inner superlayer. Because they come from loopers, late hits are often shadowed by an earlier loop, and contribute little to the occupancies described in section 5.2.

The rate calculations take account of all material inside the tracking volume, and albedo from the magnet coil, but not from the calorimeter situated beyond the coil. The charged particle rate per minimum bias event is multiplied by the interaction rate of 100 MHz at design luminosity, and simply scales with luminosity. The charged particle rate per channel at design luminosity is shown for the straw tube and gas microstrip subdetectors in table 2. These rates are relevant to questions of electronics performance and detector lifetime. Statistical errors are not quoted for rates and occupancies, since they are small compared to systematic uncertainties such as the modeling of interactions at 40 TeV.

5.2 Occupancies

For the silicon strips, straw tubes and gas microstrips, the occupancy is defined as the fraction of cells with a detected hit when the detector is triggered. The occupancy for a random trigger is proportional to the charged particle rate when the latter is low, but it differs at high rates due to pileup and deadtime effects. If the rate is increased indefinitely, the occupancy first saturates, and then falls to zero as all hits are shadowed out. In practice, the non-linearities are significant only for the straw tube subdetector at high luminosities, where the larger cell size results in higher occupancies. In contrast, the scintillating fiber readout is assumed to be continuously updating, so that there is no shadowing, but the occupancy approaches unity in the limit of high rates. Table 2 shows the occupancy for each subdetector for a random trigger at design luminosity.

We have investigated the straw tube occupancy for a Higgs event trigger as a function of luminosity ($\mathcal{L}$). This occupancy is relevant to reconstruction efficiencies. For these studies, and for the reconstruction efficiency studies of section 6, some approximations were needed to limit the computational requirements. As described in section 2.1, only particles with $|\eta| \leq 3.5$, and that originate between 6 beam crossings (approximately 100 ns) before and 2 beam crossings after the triggering beam crossing, were considered. The pseudorapidity cut and beam crossing cut cause occupancies to be underestimated by approximately 9% and 6% respectively, as determined from comparisons of random triggers at design luminosity with and without the cuts. At high luminosities, the combined effect may alternatively be interpreted as a 15% overestimate of the luminosity at which occupancies and efficiencies are measured.

The occupancy (recorded hits/wire) of the inner and outer straw superlayers is shown as a function of luminosity as solid curves in fig. 11. The mean number of charged particle hits per wire, before deadtime shadowing effects, is shown by dashed lines. The hits lost to shadowing are preferentially from low-momentum tracks that loop in the magnetic field and strike the same straw more than once. The rate and occupancy for zero luminosity correspond to hits from the Higgs event alone with no minimum bias background. For the straw tubes, the number of hits from a single Higgs event is approximately equal to the number of hits from the minimum bias background at a luminosity of 10^{33} cm^{-2}s^{-1}. More directly relevant to the physics goals of the detector is the number of good recorded hits on high-momentum tracks. Fig. 12 shows the average number of recorded hits per superlayer for a stiff muon from Higgs decay, before track reconstruction, as a function of luminosity. The maximum possible number of hits is 8 for an axial superlayer, and 6 for a stereo superlayer. The small losses at zero luminosity are mostly due to geometric effects, such as the gap between detector halves at $z = 0$, inter-straw gaps, straw walls and supports, as well as estimated electronic inefficiencies. The additional losses at higher luminosity are principally due to deadtime shadowing. The additional precision coming from the measurement of the drift time in the straw system helps to compensate for the loss of information at high luminosity due to shadowing, compared to the other tracking subdetectors. The effect of this loss of shadowed hits on segment and track reconstruction is examined in the following subsections.

5.3 Straw segment finding efficiency

Fig. 13 shows the efficiency for reconstructing a straw segment in a given superlayer and linking it to a reconstructed track, as a function of luminosity, for Higgs decay muons in the interval $0.1 < |\eta| < 1.5$. Although this is a product of track and segment reconstruction efficiencies, it is dominated by the latter. The segment reconstruction algorithm requires at least 4 out of 8 good hits for axial and 4 out of 6 good hits for stereo superlayers. The efficiency of the outer superlayer remains high beyond the SSC design luminosity, but that of the inner superlayer falls sharply, due

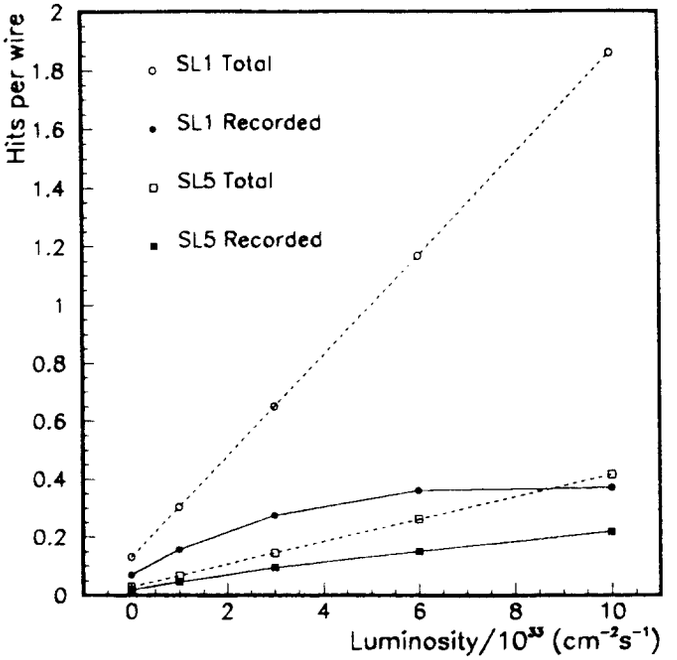

Figure 11: Mean number of recorded hits per wire (occupancy) of the inner and outer straw superlayers (SL1 and SL5) for Higgs triggers, as a function of luminosity (solid lines). The mean numbers of hits per wire, including hits not recorded due to deadtime effects, are shown connected by dashed lines.

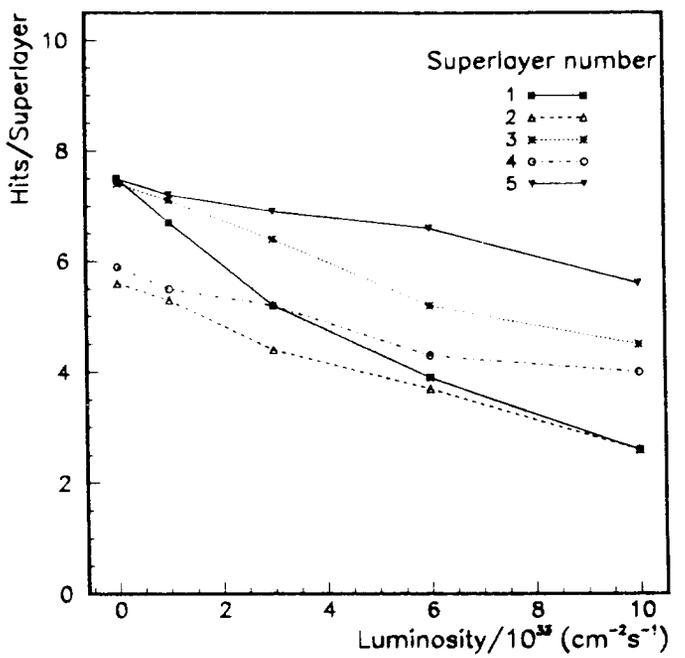

Figure 12: Mean number of recorded straw hits per superlayer for a Higgs decay muon with $p_t > 10$ GeV/c and $0.1 < |\eta| < 1.5$.

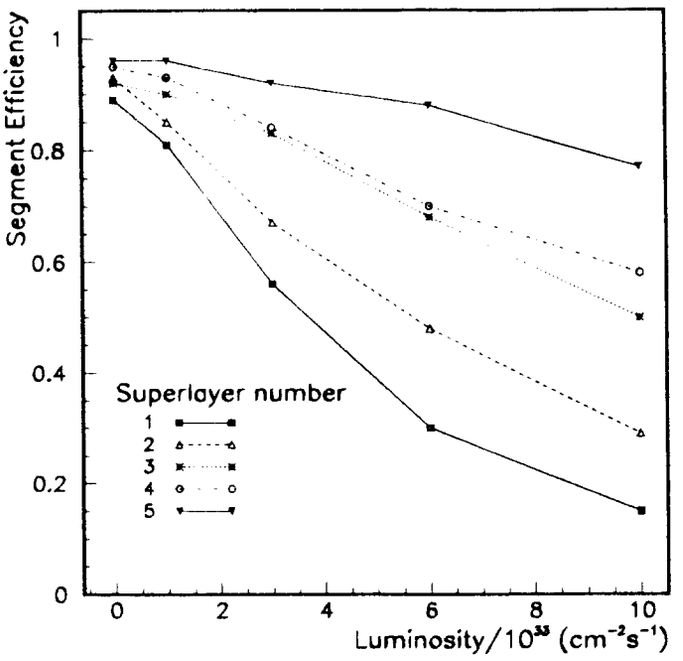

Figure 13: Efficiency for reconstructing a straw segment from a Higgs decay muon and linking it to a reconstructed track, as a function of luminosity.

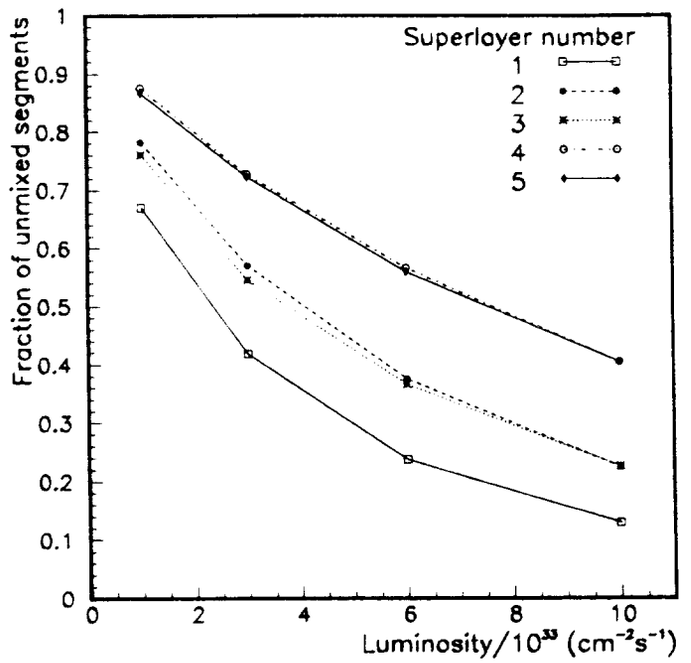

Figure 14: Fraction of unmixed segments versus luminosity for each superlayer of the straw tracker.

to both the loss of shadowed hits and to the high hit density.

The accuracy of segment reconstruction has been measured by finding the parent track that contributed the most hits to the segment, and then comparing the number of hits from that track with the total number of hits on the segment. Segments for which this fraction is high (≥ 0.75) are called "unmixed," the rest "mixed." With this definition, the fraction of segments which are unmixed is plotted in fig. 14 for all tracks of $p_t > 2$ GeV/c coming from Higgs events. For superlayers 2 and 3 at the highest luminosity, about a quarter of the segments are unmixed, compared with about 80% at design luminosity. The fraction of mixed segments is approximately independent of segment p_t, and does not cause serious problems for the subsequent track finding algorithms.

6 Overall detector performance

6.1 Definitions

Track reconstruction efficiencies are calculated by defining a set of "good" tracks at the Monte-Carlo generation level, and calculating the fraction of these for which there is a matching reconstructed track. A "good" generated track must come from the triggering beam crossing, originating at a radial distance from the beam of less than 2.5 cm. It must have $|\eta| < 2.5$ ($|\eta| < 2.25$ for the scintillating fiber detector), impact parameter $b_0 < 1$ cm and $|z_0| < 15$ cm. Results are presented for all charged particles with $p_t > 1$ GeV/c and for Higgs decay leptons with $p_t > 10$ GeV/c. A good reconstructed track must have been successfully fitted with a $\chi^2/dof < 5.0$, where dof is the number of degrees of freedom. It must have at least two measured points or one segment in both the inner (*i.e.*, silicon) and the outer tracker. A "matching" χ^2 is calculated from the measured and generated track parameters, using the error matrix of the measured parameters, which includes a contribution from multiple Coulomb scattering. To be matched to a generated track, the matching χ^2 must be less than 10^3 (10^5 for electrons, to allow for bremsstrahlung). Reconstructed tracks not so matched, or matched to a generated track that has a better match to another fitted track, are considered to be fake tracks. Reconstructed Higgs leptons that fail the matching χ^2 cut are not considered to be fake high-p_t tracks, although they are considered as reconstruction failures when calculating the track reconstruction efficiency.

The results presented in sections 6.2 through 6.8 were obtained for the baseline tracker using the zonal track finding algorithm. The segment clustering algorithm yielded similar results, with slight differences of detail due to its greater emphasis on the silicon inner tracker. Results on the performance of the scintillating fiber option using the road-following tracking algorithm are presented in section 6.9.

6.2 Reconstruction efficiency for isolated tracks

The reconstruction efficiency for isolated muons from Higgs decay at $\mathcal{L}=3 \times 10^{33}$ cm^{-2}s^{-1} is shown in fig. 15. It is high over the whole rapidity range, with slight dips at the straw tracker module boundaries near $\eta=0$ and $\eta=1.8$. There is no significant p_t dependence. The track reconstruction efficiency is plotted as a function of luminosity in fig. 16 for Higgs decay muons and for all charged particles with $p_t > 1$ GeV/c from Higgs events. The efficiency for Higgs muons is higher than for high-p_t hadrons because the latter tend to cluster in jets. Both efficiencies are high, but they start to fall off at luminosities beyond 3×10^{33} cm^{-2}s^{-1}; in particular, the efficiency for reconstructing Higgs muons meets the design criterion from section 1.2 of 97% for $\mathcal{L}=10^{33}$ cm^{-2}s^{-1}, but it falls below the one for $\mathcal{L}=10^{34}$ cm^{-2}s^{-1}.

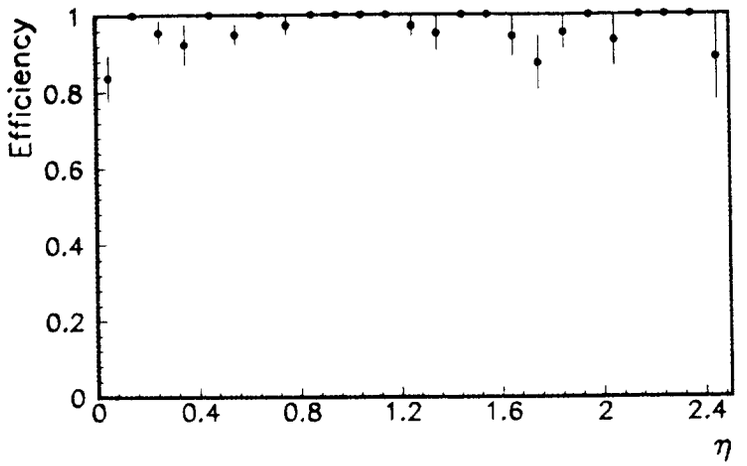

Figure 15: Track finding efficiencies as a function of pseudorapidity for Higgs muons at $\mathcal{L}=3\times10^{33}$ $cm^{-2}s^{-1}$.

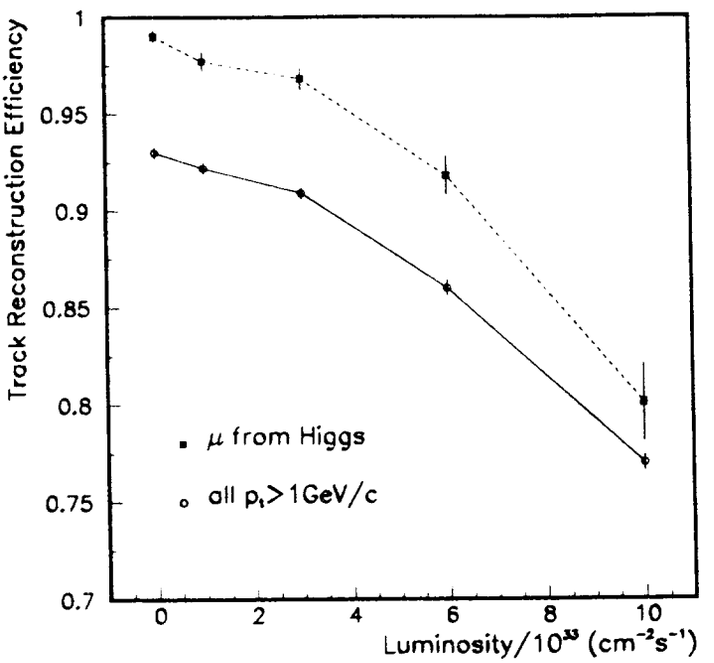

Figure 16: Track finding efficiencies as a function of luminosity for Higgs muons (solid line) and all tracks with $p_t > 1$ GeV/c (dashed line).

6.3 Fake rates

The number of fake reconstructed tracks per Higgs event is shown in fig. 17. The requirements for reconstructed tracks are very loose, in order to maximize the reconstruction efficiency, giving rates of 0.25 fake $p_t > 10$ GeV/c tracks per event at design luminosity. The fake rates can be reduced by requiring a larger number of points on a reconstructed track. For example, an approximately 50% increase in the number of points required reduces the fake rates by a factor of 5 at a luminosity of 3×10^{33} cm^{-2}s^{-1}, with only a very small decrease in the reconstruction efficiency for high-p_t tracks.

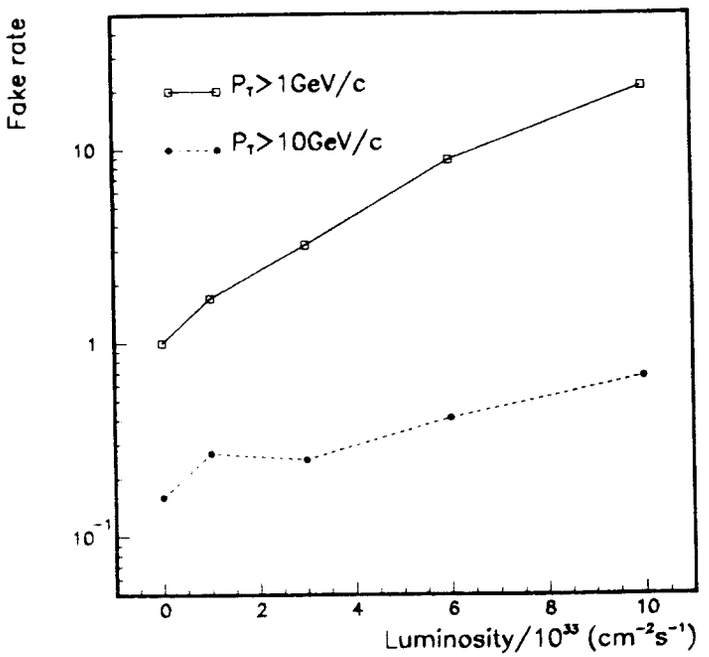

Figure 17: Number of fake tracks per event with $p_t > 10$ GeV/c (solid circles) and $p_t > 1$ GeV/c (open squares).

6.4 Resolution

Momentum, angle and position resolution have been studied by comparing generated and reconstructed track parameters for muons from Higgs decay. Unlike the reconstruction efficiency, the resolution for reconstructed tracks is not strongly luminosity dependent, and results are quoted for a luminosity of 3×10^{33} cm^{-2}s^{-1}.

Figs. 18a-c show $\Delta p_t/p_t^2$ for Higgs decay muons of $p_t > 10$ GeV/c in three pseudorapidity intervals. The tracks have not been constrained to pass through the interaction point in the transverse plane; if the beam position is known and stable, this will further improve the momentum resolution. The observed momentum resolution of $0.18 \times p_t$ (in TeV/c) in the barrel region and $0.8 \times p_t$ in the most forward region is consistent with the design goals listed in section 1.2. The small contribution from multiple Coulomb scattering to the momentum resolution in fig. 18a can be seen by comparison with fig. 18d, which shows a resolution of $0.16 \times p_t$ for muons of $p_t > 50$ GeV/c. The azimuthal angular resolution is excellent because of the requirements of momentum resolution. The resolution in dip angle λ is an order of magnitude worse, since it is measured by small angle

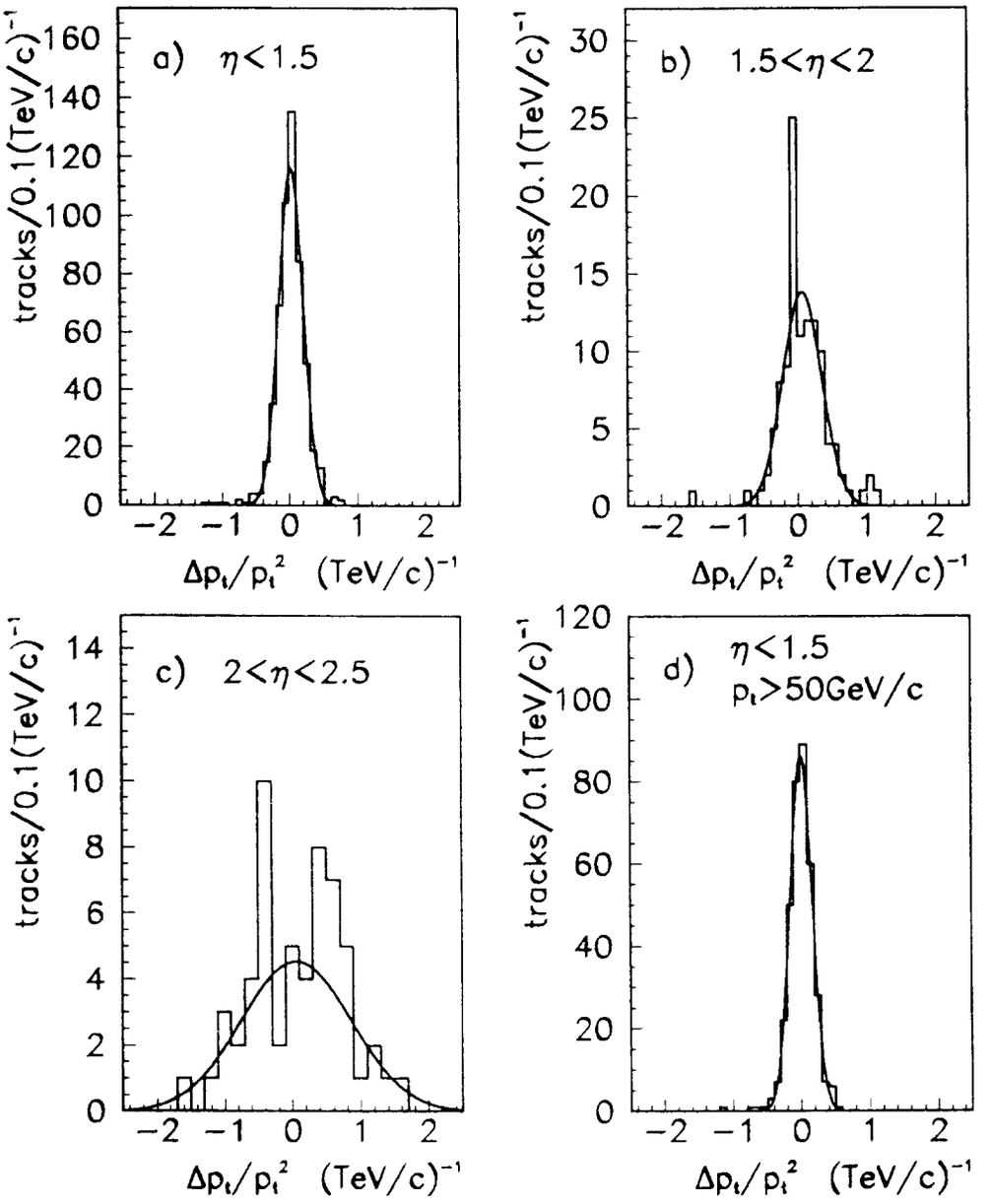

Figure 18: Fitted momentum resolution $\Delta p_t/p_t^2$ for Higgs muons at luminosity 3×10^{33} cm^{-2}s^{-1}: (a) for $|\eta| < 1.5$, $p_t > 10$ GeV/c, $\sigma = 0.18$ (TeV/c)$^{-1}$; (b) for $1.5 < |\eta| < 2.0$, $p_t > 10$ GeV/c, $\sigma = 0.29$ (TeV/c)$^{-1}$; (c) for $2.0 < |\eta| < 2.5$, $p_t > 10$ GeV/c, $\sigma = 0.81$ (TeV/c)$^{-1}$; (d) for $|\eta| < 1.5$, $p_t > 50$ GeV/c, $\sigma = 0.16$ (TeV/c)$^{-1}$.

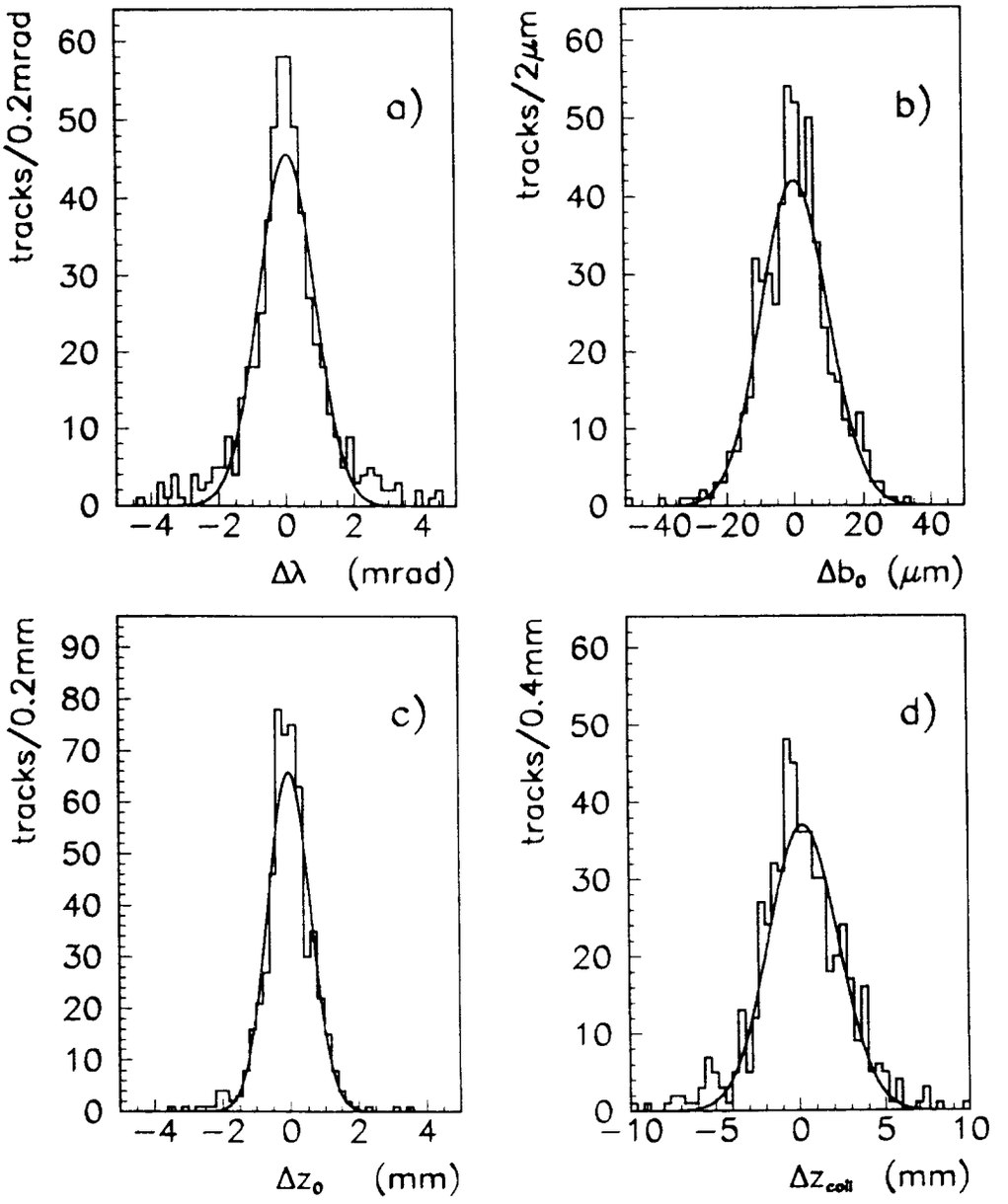

Figure 19: Fitted resolution functions for Higgs muons with $|\eta| < 1.5$ at a luminosity of 3×10^{33} $cm^{-2}s^{-1}$: (a) in λ, the dip angle, $\sigma = 0.8$ mrad, (b) in b_0, the impact parameter, $\sigma = 10\mu$m, (c) the z_0 resolution at the vertex, $\sigma = 0.6$ mm and (d) the z resolution at the coil face, $\sigma = 2.0$ mm.

stereo; it is roughly 1 mrad, as illustrated in fig. 19a. The transverse impact parameter resolution of fig. 19b is about 10 microns. The z coordinate resolution for a single track extrapolated back to the vertex is less than 1 mm (fig. 19c), which more than satisfies the design requirement for vertexing. The z resolution at the coil face, important for matching to the calorimeters and muon chambers, meets the design goal of 2.5 mm as shown in fig. 19d. It could perhaps be improved further by moving the second stereo straw layer out to larger radius. The outer tracker is essential for achieving the resolution requirements of section 1.2. For example, with the silicon inner tracker alone, the momentum resolution in the barrel region would be approximately $0.7 \times p_t$ (in TeV/c), and the z resolution at the coil face would also deteriorate substantially.

6.5 Electron efficiency and resolution

The track reconstruction efficiency for electrons depends on how accurate a momentum measurement is required, *i.e.*, how much bremsstrahlung is acceptable. The SDC calorimeter response was not simulated in this study, and we replace the usual cut on p/E (tracker momentum/calorimeter energy) by a cut on (tracker momentum/generated momentum), since the calorimeter measurement is expected to be much more accurate than the tracker measurement. The results below were obtained by fitting the entire observed electron track. It may be possible to reduce sensitivity to bremsstrahlung, at some cost in measurement error, by fitting an assumed bremsstrahlung, or by fitting only the early part of the track, for example, the silicon strip measurements only.

Fig. 20 shows the track reconstruction efficiency for Higgs electrons for various p/E cuts. The choice of cut will depend on the background levels to electron identification. The effect of the additional material (cables, services and supports) situated between the barrel straw tracker and the intermediate-angle gas microstrip tracker is reflected in the lower efficiency for the region $1.5 < |\eta| < 2.0$ once a p/E cut is applied.

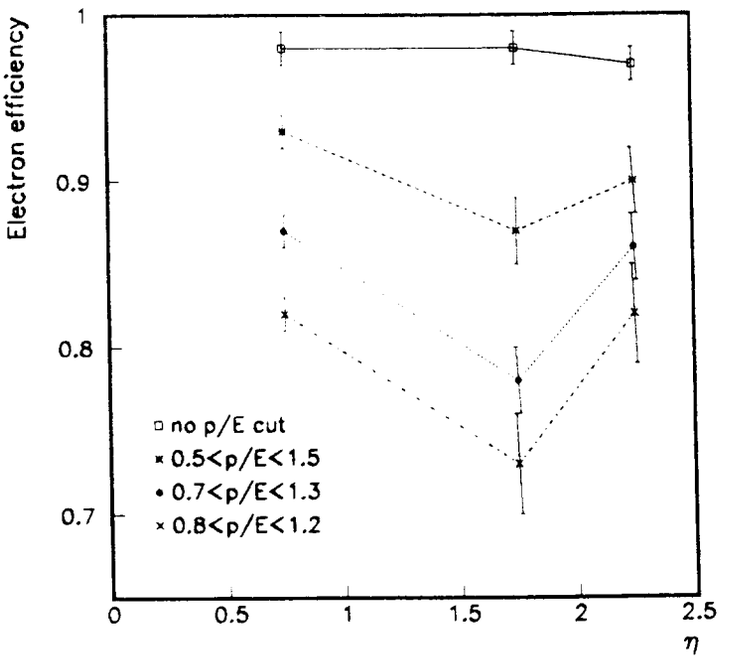

Figure 20: Track finding efficiencies for Higgs electrons for various p/E cuts.

91% to 79% for all tracks with $p_t > 1$ GeV/c and $|\eta| < 2.5$. The reconstruction efficiency for all tracks with $p_t > 1$ GeV/c is shown as a function of pseudorapidity in fig. 23. As expected, the effect is greatest at the highest rapidities, where the most measurements are lost.

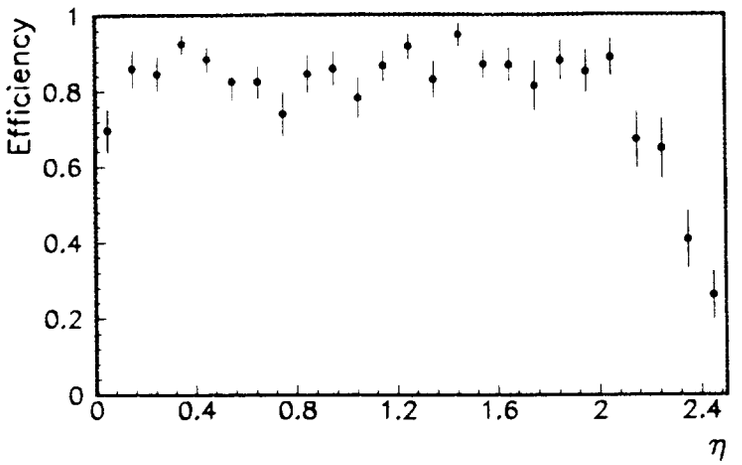

Figure 23: Track finding efficiencies as a function of pseudorapidity for all tracks with $p_t > 1$ GeV/c in a tracking system with a descoped silicon tracker

6.9 Reconstruction efficiency for scintillating fiber option

The performance of the scintillating fiber option (fig. 1b) was also investigated using a sample of Higgs events as described in section 2.1. Reconstruction was performed with the road-following algorithm described in section 4.7.2. The track reconstruction efficiency has been studied as a function of luminosity for muons, electrons and hadrons originating from the primary vertex. A reconstructed track must not cross more than two consecutive layers without hits, but it is not required to have hits in the scintillating fiber outer tracker if $|\eta| \geq 2.25$. The efficiency was calculated for electrons and muons with $p_t > 5$ GeV/c and for hadrons with $p_t > 2$ GeV/c. The muon and hadron efficiencies require the matching χ^2 to be below 1000 and cover the range $|\eta| < 2.5$. The electrons are required to have $p/E > 0.5$, where E is the Monte Carlo energy and p is the measured track momentum. The electron efficiency is calculated for $|\eta| < 1.55$, corresponding to the acceptance of the outer fiber superlayer. The efficiencies, shown in fig. 24, are high and show little or no decrease as the luminosity is increased from zero to ten times the SSC design value of 10^{33} cm^{-2}s^{-1}. The electron efficiency is found to increase at the highest luminosity, probably because tracks that bremsstrahlung in the outer tracker can pick up noise hits close to their original trajectory. Initially, a few percent of the tracks at high luminosity were found to be poorly reconstructed in the z-coordinate and dip angle. This occurred because the tracks were picking up wrong hits in the scintillating fiber stereo layers. It was corrected by eliminating all fiber stereo hits from tracks with fewer than three hits in the four stereo fiber layers. This suggests that the system has minimal redundancy in the fiber stereo and that it may be necessary to add more

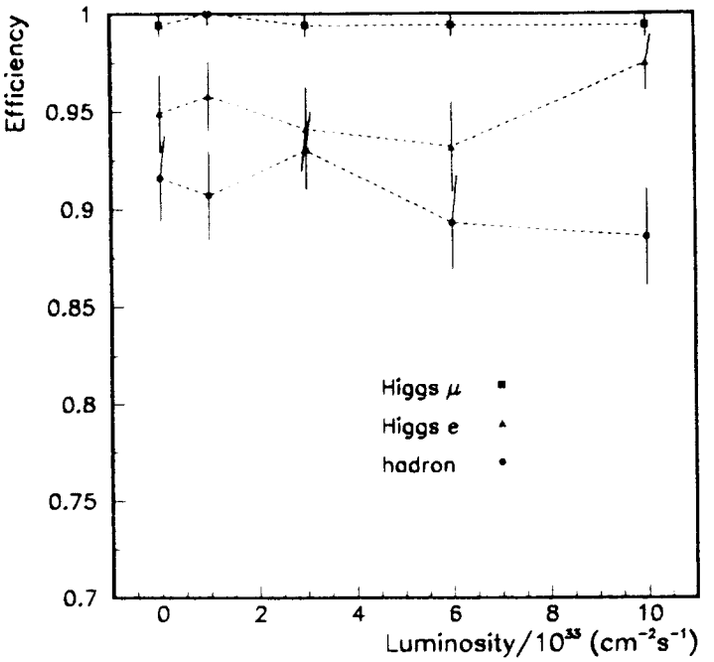

Figure 24: Muon, electron and hadron reconstruction efficiencies as a function of luminosity for $H \to Z^0\ Z^0 \to \mu^+\mu^-\ e^+e^-$ events in the scintillating fiber option.

such measurements to remove ambiguities and obtain the ultimate z resolution for all tracks. The scintillating fiber efficiencies in fig. 24 may be compared with the straw/ITD results in fig. 16. The efficiencies are similar at low luminosity but the fiber system shows significantly less degradation at high luminosity because of its finer granularity and faster response. The resolutions for the fiber system are not shown, but they are comparable to those shown for the baseline tracking design, except in the forward region $|\eta| > 2.0$, where the gas microstrip ITD provides a better measurement.

6.10 Reconstruction efficiency for tracks in jets

The ability of the SDC tracking system to reconstruct tracks in high p_t jets has been investigated, with the goal of being able to tag b or c quark jets via their decay into muons. This physics process makes severe demands on the two-track resolution of the tracking system and the reconstruction algorithms in order to reconstruct tracks accurately in the locally dense environment near the core of a high-p_t jet.

To study this process, the ISAJET Monte Carlo program was used to generate samples of events containing two b jets with minimum p_t of 25, 100, 200 and 500 GeV/c. In one of the jets, any B meson was required to decay semileptonically yielding a muon. Higher order effects such as gluon radiation sometimes produce additional jets, whose p_t may be greater than or less than the original minimum jet p_t. The detector simulation was carried out at the design luminosity of 10^{33} $cm^{-2}s^{-1}$ as described in section 2.1. Near the core of a jet, the occupancy comes predominantly from the jet tracks themselves, and not from pileup; in tests, no significant dependence of reconstruction efficiency on luminosity or background hits was observed. The jet axes and momenta were calculated from the generated Monte Carlo particles, both charged and neutral, using a momentum clustering algorithm that combines particles within a cone size of $\Delta R < 0.5$, where $\Delta R = \sqrt{\Delta\eta^2 + \Delta\phi^2}$.

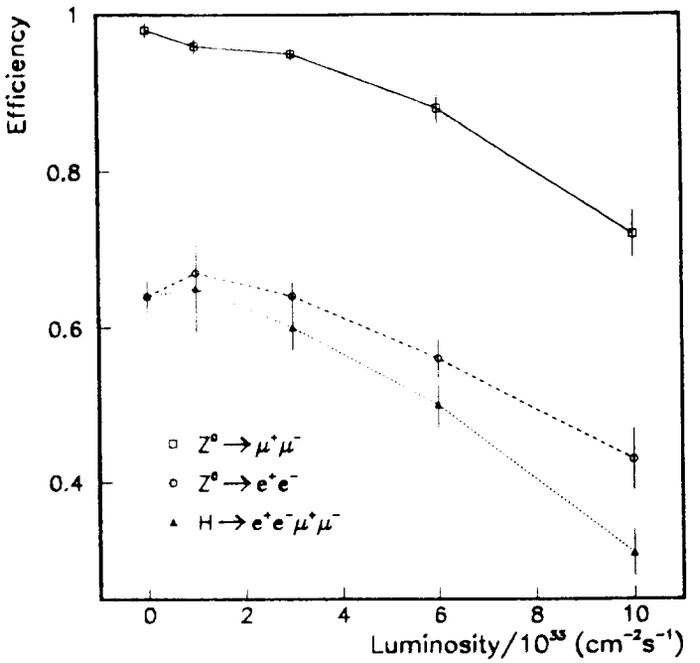

Figure 22: Z^0 and Higgs reconstruction efficiencies: solid line: $Z^0 \rightarrow \mu^+\mu^-$ efficiency; dashed line: $Z^0 \rightarrow e^+e^-$ efficiency; dotted line: H $\rightarrow$ Z^0 $Z^0 \rightarrow \mu^+\mu^-$ e^+e^- efficiency.

leptons to lie within $|\eta| < 2.5$. Their values reflect the track reconstruction efficiencies and the p/E cut for electrons. It is possible that the electron identification criteria could be relaxed and the efficiency increased when part of a four-lepton event. Nevertheless, the Higgs reconstruction efficiency is high, and remains substantial even at the very high luminosity of 10^{34} $cm^{-2}s^{-1}$.

6.7 Variations in neutron background

A test has been made of the sensitivity of the track finding and reconstruction to unexpectedly high neutron and photon background levels. The simulation at 3×10^{33} $cm^{-2}s^{-1}$ luminosity has been repeated with 10 times the expected neutron and photon backgrounds. This increases both the random "noise" hits and the number of good hits lost to shadowing. The overall muon reconstruction efficiency was observed to fall by 1%, and the fake rate approximately doubled. We conclude that the system retains a safety margin with respect to unexpectedly high random backgrounds or inefficiencies.

6.8 Reduced silicon system

The consequences of a reduction in scope of the tracking system have been considered. Such a situation could arise, for example, if detector construction were staged due to budgetary pressures, or as a result of a partial breakdown or radiation damage. We have studied the reconstruction efficiency for high-p_t tracks at a luminosity of 3×10^{33} $cm^{-2}s^{-1}$ for a tracking system with the silicon subsystem modified by removing the four inner barrel superlayers and the four outer disks of each forward arm. Compared to a tracker with a complete silicon system, this results in a reduction from 97% to 90% in the reconstruction efficiency for muons from Higgs bosons, and from

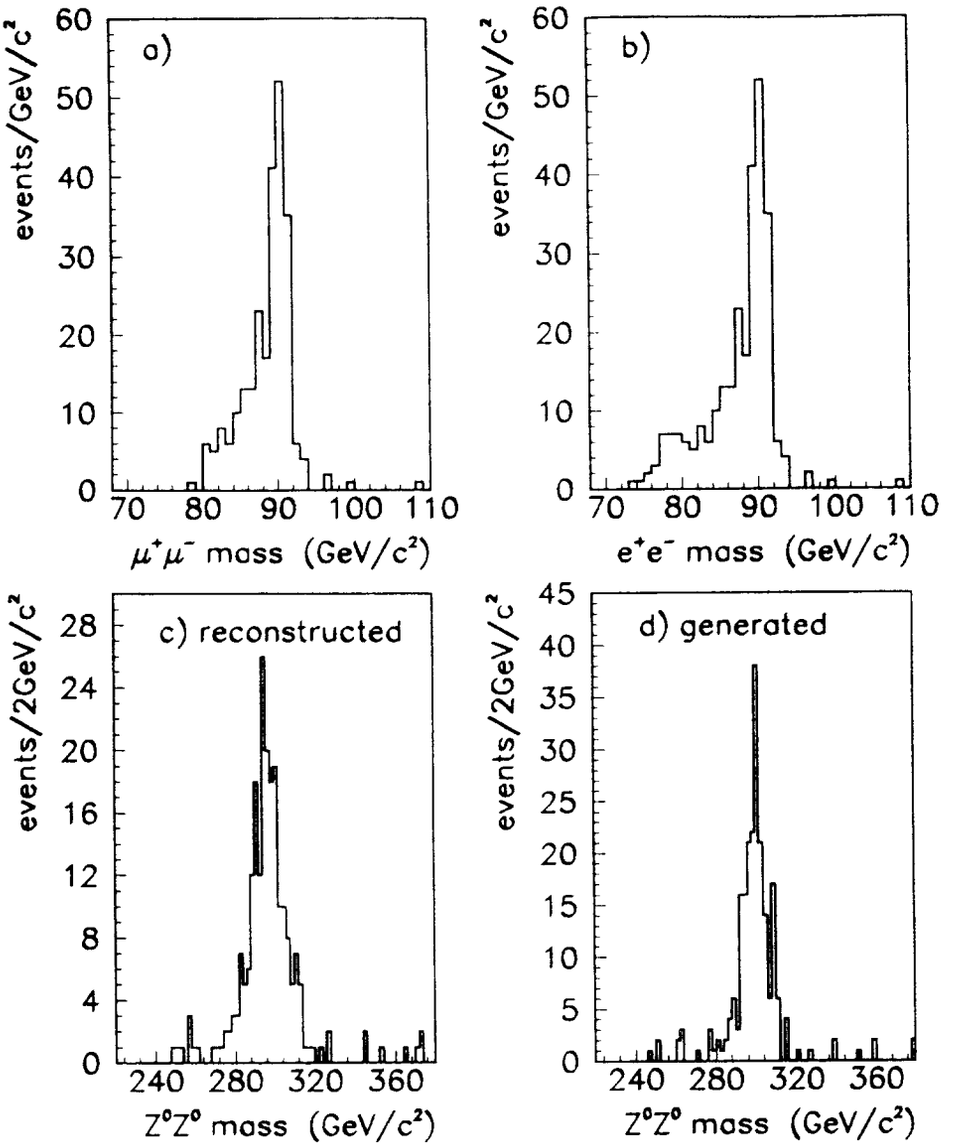

Figure 21: Z^0 and Higgs mass resolution: (a) $\mu^+\mu^-$ effective mass, (b) e^+e^- effective mass, (c) reconstructed Z^0Z^0 effective mass, and (d) generated Z^0Z^0 effective mass.

6.6 Z^0 and higgs reconstruction

The reconstructed $\mu^+\mu^-$ effective mass distribution for Higgs events (without background processes) is shown in fig. 21a. This corresponds to a Z^0 mass resolution of approximately 3 GeV/c^2. The corresponding distribution in fig. 21b for electron pairs having $p/E > 0.7$ still shows a tail at low masses due to electron bremsstrahlung. In the full experiment, this would be improved by using the calorimetric measurement of electron energy. Lepton pairs with masses between 81 and 101 GeV/c^2 are taken as Z^0 candidates. The reconstructed Z^0 pair effective mass is shown in fig. 21c. A Gaussian fit to the mass interval 280-320 GeV/c^2, which excludes the Breit Wigner tails of the Higgs, yields an apparent resolution of approximately 8 GeV/c^2 on the Higgs mass, to be compared with a contribution of 6 GeV/c^2 from the natural width (fig. 21d). The Z^0 and Higgs reconstruction efficiencies for the above cuts are plotted as a function of luminosity in fig. 22. The Higgs efficiencies do not include the geometrical acceptance of approximately 55% for all four

Efficiencies were measured using a set of "good" tracks defined as in section 6.1, with the additional requirement that the track have $p_t > 2$ GeV/c and be assigned to a jet within $\Delta R < 0.5$. The track finding algorithms used were the road-following algorithm for the scintillating fiber option and the segment-clustering algorithm for the straw tube plus gas microstrip design. Preliminary studies using the zonal algorithm showed results similar to the segment-clustering method for this physics process.

The track reconstruction efficiency is shown as a function of the p_t of the jet containing that Monte Carlo track, for all tracks with $p_t > 2$ GeV/c in fig. 25a, and separately for the muon from the semileptonic decay in fig. 25b. Both tracking options comfortably meet the design requirements of section 1.2. The efficiency for the straw tube system starts to fall beyond a jet p_t of 500 GeV/c, whereas the fiber tracking system maintains good efficiency out to a jet p_t of 1 TeV/c. One can also look at the track reconstruction efficiency as the track approaches the center of the jet core. Fig. 26 shows the efficiency as a function of ΔR, the distance of the track from the center of the jet, for two ranges of jet p_t. The straw and gas microstrip option with the segment-clustering algorithm shows a loss of efficiency close to the jet core for $p_t^{jet} > 200$ GeV/c.

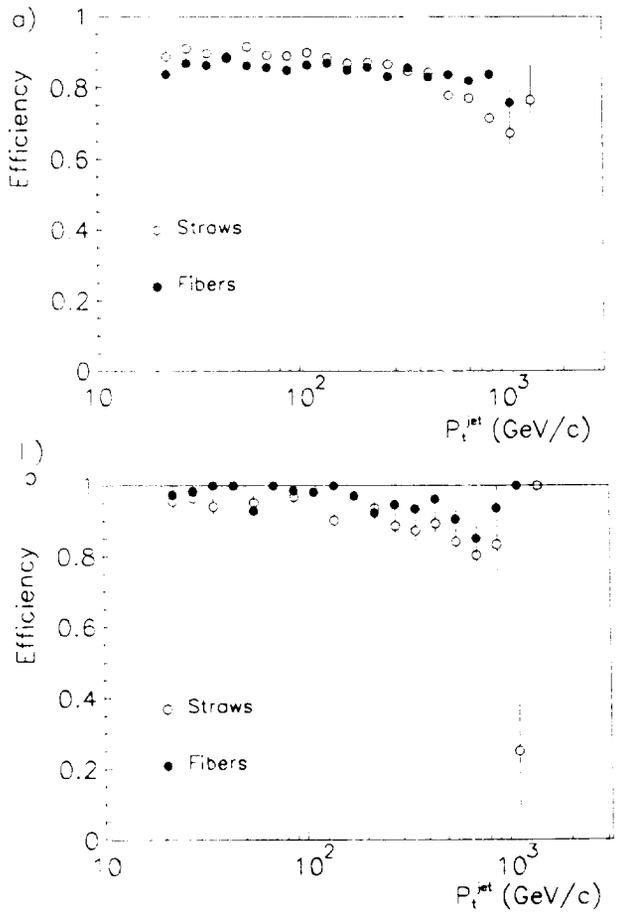

Figure 25: Track reconstruction efficiency versus jet p_t for a) all tracks in jet with $p_t > 2$ GeV/c, and b) the muon from the semileptonic decay, for straw and gas microstrip (open circles) and scintillating fiber (solid circles) options.

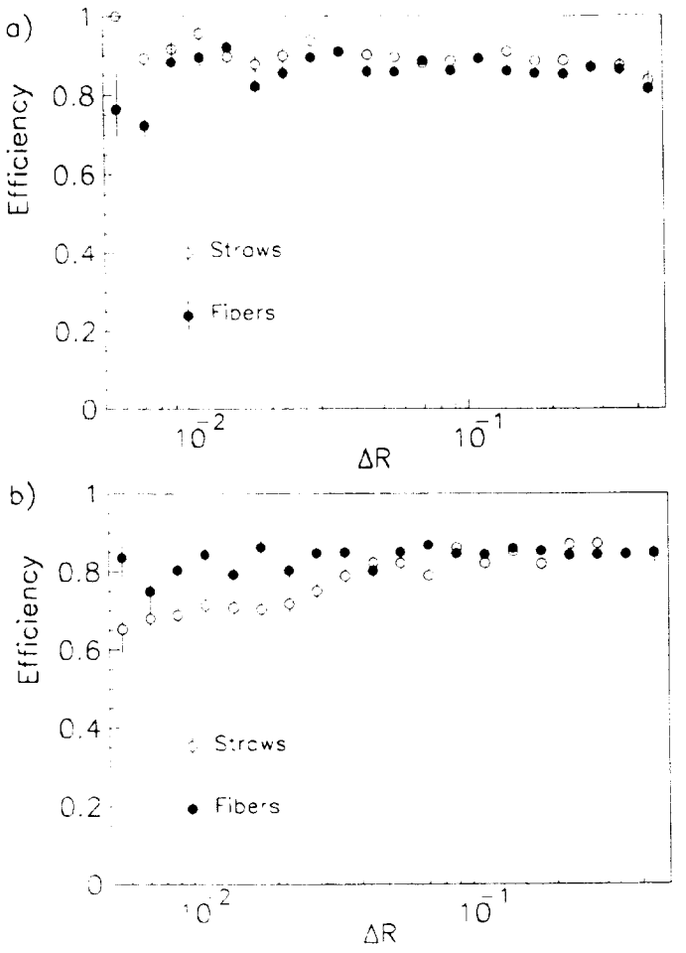

Figure 26: Track reconstruction efficiency versus distance of track from center of jet, $\Delta R = \sqrt{\Delta\eta^2 + \Delta\phi^2}$, for a) jets with $p_t < 200$ GeV/c, and b) jets with $p_t > 200$ GeV/c, for straw and gas microstrip (open circles) and scintillating fiber (solid circles) options.

Both tracking designs with their respective reconstruction algorithms already meet the somewhat modest requirements of section 1.2 for tracking in jets. Other physics processes not examined here, (B meson physics, for example), may demand increased efficiency. Preliminary studies indicate that further optimization of the reconstruction algorithms may be possible for both tracking options.

7 Conclusions

Simulation studies have been carried out to evaluate the whole-system performance of tracking detector designs for the SDC experiment for the Superconducting Super Collider. System performance was compared to requirements derived from the physics aims of the experiment. Results show that these requirements can be met provided that the individual detector elements perform as described in section 3.

Both versions of the tracker described above perform well at the SSC design luminosity of 10^{33}

$cm^{-2}s^{-1}$. They retain substantial tracking capability at considerably higher luminosities; however, the inner superlayers of the straw tracking system show a steady degradation of performance with increasing luminosity.

In order for a straw tracker to be fully viable at a luminosity of 10^{34} $cm^{-2}s^{-1}$, for example, at the LHC, ways must be found to reduce the occupancy of individual straws. This might be achieved by using shorter straws and by further reducing the sensitivity to loopers by using a lower magnetic field or non-axial straws. The other tracker components performed adequately at this luminosity.

Acknowledgements

This work was supported in part by the Texas National Research Laboratory Commission, by the U.S. Department of Energy, including contract numbers DE-FG02-91ER40672, DE-FG03-92ER40689, DE-FG05-91ER40665, DE-FG05-92ER40742, DE-FC05-85ER250000, DE-FG02-91ER40661, DE-AC02-84ER40125, by the Natural Sciences and Engineering Research Council of Canada, and by the US-Japan High Energy cooperation program of the Ministry of Education, Culture and Science, Japan.

References

[1] Technical Design Report. Solenoidal Detector Collaboration, April 1992, SSCL-SR-1215.

[2] The Compact Muon Solenoid Technical Proposal, CERN/LHCC 94-38.

[3] ATLAS Technical Proposal for a General-Purpose pp Experiment at the Large Hadron Collider at CERN, CERN/LHCC 94-43.

[4] F.Luehring et al., "Simulation of the TRT System Rate Response and Occupancy", Atlas Internal Note: INDET-NO-81, 20-Dec-94, and other private communications.

[5] GEANT Detector Description and Simulation Tool, CERN Program Library Q123.

[6] F. E. Paige and S. D. Protopopescu, **BNL-38034**, 1986.

[7] T. Sjostrand, *PYTHIA 5.6 and JETSET 7.3 Physics and Manual*, **CERN-TH.6488/92**, May 1992.

[8] G. Eppley at al., SDC note SDC-92-217.

[9] A straw drift tube outer tracking system for the Solenoidal Detector Collaboration experiment at the SSC, in preparation.

[10] D. Rust, private communication from Neutron Background Task Force.

[11] R. Fruhwirth, Nucl. Instr. and Meth. A262 (1987) 444 and references therein.